Department of Electrical Engineering and Automation

Quality, Microstructural Refinement and Stability of Atomic-Layer-Deposited Aluminum Nitride and Aluminum Oxide Films

Mikael Broas



Aalto University

DOCTORAL DISSERTATIONS

Aalto University publication series
DOCTORAL DISSERTATIONS 151/2018

Quality, Microstructural Refinement and Stability of Atomic-Layer-Deposited Aluminum Nitride and Aluminum Oxide Films

Mikael Broas

A doctoral dissertation completed for the degree of Doctor of Science (Technology) to be defended, with the permission of the Aalto University School of Electrical Engineering, at a public examination held at the lecture hall TU1 of the school on 13 September 2018 at noon.

Aalto University
School of Electrical Engineering
Department of Electrical Engineering and Automation
Unit of Electronics Integration and Reliability

Supervising professor
Professor Mervi Paulasto-Kröckel, Aalto University, Finland

Thesis advisor
Dr. Vesa Vuorinen, Aalto University, Finland

Preliminary examiners
Professor Ingrid De Wolf, Imec/KU Leuven, Belgium
Professor Paul H. Mayrhofer, TU Wien, Austria

Opponents
Professor Markku Leskelä, University of Helsinki, Finland
Dr. Achim Trampert, Paul Drude Institute for Solid State Electronics, Germany

Aalto University publication series
DOCTORAL DISSERTATIONS 151/2018

© 2018 Mikael Broas

ISBN 978-952-60-8129-8 (printed)
ISBN 978-952-60-8130-4 (pdf)
ISSN 1799-4934 (printed)
ISSN 1799-4942 (pdf)
http://urn.fi/URN:ISBN:978-952-60-8130-4

Unigrafia Oy
Helsinki 2018

Finland

441 697
Printed matter

Aalto University

Abstract

Aalto University, P.O. Box 11000, FI-00076 Aalto www.aalto.fi

Author
Mikael Broas

Name of the doctoral dissertation
Quality, Microstructural Refinement and Stability of Atomic-Layer-Deposited Aluminum Nitride and Aluminum Oxide Films

Publisher School of Electrical Engineering

Unit Department of Electrical Engineering and Automation

Series Aalto University publication series DOCTORAL DISSERTATIONS 151/2018

Field of research Electronics integration and reliability

Manuscript submitted 19 April 2018 **Date of the defence** 13 September 2018

Permission to publish granted (date) 9 August 2018 **Language** English

☐ **Monograph** ☒ **Article dissertation** ☐ **Essay dissertation**

Abstract

High-quality, stable ALD films are required in microelectronics when the films are exposed to further processing during device manufacturing, or if the films are exposed to a demanding environment. For example, front-end-of-line processing exposes the deposited materials to high temperatures and aggressive chemicals during process steps such as dopant activation and wafer cleaning. Furthermore, a protective film against humidity and corrosion may need to maintain its structural integrity for the lifetime of the device which can be several years. Therefore, engineering the film quality and understanding the effects of high-temperature processing on thin films are required for the successful integration of the films to a semiconductor device. The goal of this thesis was to study the quality, microstructural refinement, and the stability of ALD AlN and Al_2O_3 films. The results were divided to the process development of ALD AlN and Al_2O_3 films, the examination of their microstructural development due to high-temperature thermal treatments, and the resulting stability of the ALD films. Film stability was understood to encompass thermal stability (e.g. oxidation) and chemical stability (ability to resist dissolution and corrosion). Film quality comprised of attributes such as the amount of impurities, stoichiometry, and crystallinity which were characterized for the as-deposited films and after the high-temperature treatments.

The emphasis on ALD AlN was in process development. Trimethylaluminum (TMA) -based AlN was amorphous and contained a high amount of hydrogen when deposited at 200 °C. The hydrogen outgassed during high-temperature treatments and the AlN films began to oxidize at and above 800 °C. $AlCl_3$-based AlN films, processed closer to 500 °C, had less impurities and a polycrystalline microstructure as opposed to the TMA-based films deposited at 200 °C. The AlN film residual stress was also tunable in the plasma-enhanced $AlCl_3$ process by adjusting the plasma time of the nitrogen precursor. ALD AlN studied in this thesis and the literature review show promise of the film quality continuously improving. The main challenges are in improving the crystalline quality and minimizing the amount of impurities, such as hydrogen, in the AlN films.

The focus on ALD Al_2O_3 was in understanding the effects of the high-temperature treatments. As-deposited ALD Al_2O_3 was amorphous and dissolved into wet chemical cleaning solutions. Heat treatments at and above 800 °C crystallized the films. However, high vacuum annealing caused blistering of the alumina films, whereas atmospheres with hydrogen and nitrogen produced crystalline films without blisters. The fully-crystallized alumina films were stable in SC-1 and HF cleaning solutions. The crystallized alumina films are demonstrated to be suitable for technologies such as silicon on insulator. Furthermore, crystallized ALD alumina could be utilized as a protective layer in a variety of applications that withstand the crystallization temperature.

Keywords atomic layer deposition, annealing, thin film stability, AlN, Al2O3, microstructure, impurities, stoichiometry, transmission electron microscopy

ISBN (printed) 978-952-60-8129-8 **ISBN (pdf)** 978-952-60-8130-4

ISSN (printed) 1799-4934 **ISSN (pdf)** 1799-4942

Location of publisher Helsinki **Location of printing** Helsinki **Year** 2018

Pages 150 **urn** http://urn.fi/URN:ISBN:978-952-60-8130-4

Aalto-yliopisto

Tiivistelmä

Aalto-yliopisto, PL 11000, 00076 Aalto www.aalto.fi

Tekijä
Mikael Broas

Väitöskirjan nimi
Atomikerroskasvatettujen alumiininitridi- ja alumiinioksidikalvojen laatu, mikrorakenteellinen muokkaus ja stabiilisuus

Julkaisija Sähkötekniikan korkeakoulu

Yksikkö Sähkötekniikan ja automaation laitos

Sarja Aalto University publication series DOCTORAL DISSERTATIONS 151/2018

Tutkimusala Elektroniikan integrointi ja luotettavuus

Käsikirjoituksen pvm 19.04.2018 **Väitöspäivä** 13.09.2018

Julkaisuluvan myöntämispäivä 09.08.2018 **Kieli** Englanti

☐ **Monografia** ☒ **Artikkeliväitöskirja** ☐ **Esseeväitöskirja**

Tiivistelmä

Mikroelektroniikan valmistuksessa käytettävien kalvojen täytyy olla korkealaatuisia ja stabiileja, erityisesti jos kalvot pinnoitetaan prosessoinnin alkuvaiheessa tai jos kalvot altistuvat käytön aikana aggressiiviselle ympäristölle. Esimerkiksi valmistuksen alkupäässä pinnoitetut materiaalit altistuvat korkeille lämpötiloille ja aggressiivisille kemikaaleille seosteiden aktivoinnin ja kiekkopesujen aikana. Kosteudelta ja korroosiolta suojaavan kalvon täytyy pysyä ehjänä tuotteen elinkaaren ajan, joka voi olla useita vuosia. Ohutkalvojen laadun muokkaus ja ymmärrys korkealämpökäsittelyjen vaikutuksesta kalvojen rakenteeseen ovat edellytyksenä kalvojen käyttöön teollisessa mikroelektroniikan valmistuksessa. Tämän väitöstyön tavoitteena oli tutkia atomikerroskasvatettujen AlN- ja Al_2O_3-kalvojen laatua, mikrorakenteen muokkausta ja stabiilisuutta. Tulokset jaettiin AlN- ja Al_2O_3-kalvojen prosessikehitykseen, mikrorakenteen kehittymisen tarkasteluun lämpökäsittelyjen seurauksena ja kyseisten ALD-kalvojen stabiilisuuteen. Kalvojen stabiilisuutta käsiteltiin termisen stabiliteetin (esim. hapettuminen) ja kemiallisen stabiliteetin (kyky vastustaa liukenemista ja korroosiota) kannalta. Kalvojen laatu käsitti ominaisuuksia kuten epäpuhtauksien määrän, stoikiometrian ja kiteisyyden, jotka karakterisoitiin kasvatuksen ja lämpökäsittelyjen jälkeen.

AlN:n tarkastelu painottui prosessikehitykseen. Trimetyylialumiiniin pohjautuvat AlN-kalvot olivat kasvatuksen jälkeen amorfisia ja sisälsivät runsaasti vetyä, kun kasvatus tapahtui 200 °C:ssa. Lämpökäsittelyjen seurauksena vedyn määrä kalvoissa väheni huomattavasti, mutta AlN-kalvot alkoivat hapettua 800 °C:ssa. Lähellä 500 °C:ta kasvatetut $AlCl_3$:een perustuvat AlN-kalvot olivat monikiteisiä ja sisälsivät vähemmän epäpuhtauksia kuin 200 °C:ssa kasvatetut trimetyylialumiinipohjaiset kalvot. $AlCl_3$-pohjaisten AlN-kalvojen jännitystilaa oli lisäksi mahdollista muokata plasmapohjaisella prosessilla säätämällä typpiprekursorin plasmapulssin aikaa. Tässä työssä kasvatetun AlN:n ja kirjallisuuskatsauksen perusteella AlN:n prosessointi kehittyy jatkuvasti ja kalvojen laadun voidaan odottaa paranevan tulevaisuudessa. Kidelaadun parantaminen ja epäpuhtauksien minimointi AlN-kalvoissa ovat tämänhetkisiä tärkeimpiä haasteita.

Al_2O_3:n tarkastelu painottui lämpökäsittelyjen vaikutusten ymmärtämiseen. Kasvatuksen jälkeiset Al_2O_3-kalvot olivat amorfisia ja liukenivat puhdistuskemikaaleihin. Lämpökäsittely yli 800 °C:ssa kiteytti alumiinioksidin. Korkeatyhjiössä hehkutus kuitenkin aiheutti alumiinioksidissa rakkuloitumista. Vetyä tai typpeä sisältävässä suojakaasuhehkutuksessa rakkuloita ei havaittu. Täysin kiteytyneet Al_2O_3-kalvot olivat stabiileja SC-1- ja HF-liuoksissa. Kiteytettyjen aloksikalvojen käyttöä demonstroidaan pii eristeen päällä -teknologiassa. Kiteytettyjä aloksikalvoja voitaisiin käyttää myös suojaavana pinnoitteena sovelluksissa, jotka kestävät kalvon kiteytymislämpötilan.

Avainsanat atomikerroskasvatus, korkealämpökäsittely, ohutkalvon stabiilisuus, AlN, Al2O3, mikrorakenne, epäpuhtaudet, stoikiometria, läpivalaisuelektronimikroskopia

ISBN (painettu) 978-952-60-8129-8 **ISBN (pdf)** 978-952-60-8130-4

ISSN (painettu) 1799-4934 **ISSN (pdf)** 1799-4942

Julkaisupaikka Helsinki **Painopaikka** Helsinki **Vuosi** 2018

Sivumäärä 150 **urn** http://urn.fi/URN:ISBN:978-952-60-8130-4

Acknowledgements

This research was conducted at Aalto University in the Electronics Integration and Reliability Unit of the Department of Electrical Engineering and Automation. The work was financially supported by ECSEL2014-2-662155 project: Informed and by the Aalto ELEC Doctoral School. In addition, Fraunhofer IMWS – Center for Applied Microstructure Diagnostics provided support in the form of facilities, analysis, and instrument training. Fulbright Finland is acknowledged for the financial support to study at the Georgia Institute of Technology. Most of the experimental results were obtained in the facilities of OtaNano, Aalto University and the University of Jyväskylä.

I am forever grateful to my supervisor Professor Mervi Paulasto-Kröckel for her guidance and support regarding the thesis work and other professional endeavors. I express my gratitude to Dr. Vesa Vuorinen for being my instructor and for all the helpful discussions we had.

There are so many additional colleagues who collaborated with this and other research, provided academic counseling, and helped me master various tools. In no particular order I would like to express my gratitude to Professor Matthias Petzold, Mr. Markku Tilli, Mr. Frank Altmann, Professor Timo Sajavaara, Dr. Andreas Graff, Dr. David Poppitz, Dr. Ulla Vainio, Mr. Perttu Sippola, Mr. Ville Rontu, Dr. Hua Jiang, Dr. Toni Mattila, Dr. Jussi Hokka, Dr. Jue Li, Dr. Hongqun Dong, Mr. Antti Rautiainen, Mr. Glenn Ross, Mr. Elmeri Österlund, Mr. Olli Kanninen, Mr. Nikolai Mäntyoja, Dr. Alexander Pyymäki Perros, Dr. Sami Suihkonen, Mr. Jori Lemettinen, Dr. Yanling Ge, and Dr. Xuwen Liu.

Finally, no thesis would be possible without the support of an encouraging family.

Munich, Germany, April 2018
Mikael Broas

Contents

Acknowledgements 1
List of Abbreviations and Symbols 5
List of Publications 7
Author's Contribution 8
1. Introduction 9
2. Thin Film Processing–Quality Relationships 13
3. Atomic Layer Deposition 17
3.1 Principle, Stoichiometry and Impurities 17
3.2 ALD Aluminum Nitride 19
3.3 ALD Aluminum Oxide 22
3.4 Microstructure 23
4. Structural and Chemical Characterization Methods of Thin Films 27
4.1 Electron Microscopy 27
4.1.1 Electron Diffraction 30
4.1.2 Diffraction Contrast Imaging 32
4.1.3 Phase-contrast Imaging 33
4.1.4 STEM, EDX and NBED 34
4.2 X-ray Diffraction and Reflectivity 36
4.3 Time-of-flight Elastic Recoil Detection Analysis 38
5. ALD Film Stability 41
5.1 Thermal Budget 41
5.2 Thermal Stability 42
5.3 Chemical Stability 47
5.4 Crystallization 49
6. Prospects 55
7. Conclusions 59
References 61
Publications 69

List of Abbreviations and Symbols

ALD	Atomic layer deposition, atomic-layer-deposited
BF	Bright-field
BOX	Buried oxide
BSE	Back-scattered electrons
CBED	Converged electron beam diffraction
CCD	Charge-coupled device
CMOS	Complementary metal-oxide-semiconductor
CVD	Chemical vapor deposition
DF	Dark-field
DIW	De-ionized water
DSC	Differential scanning calorimetry
ED	Electron diffraction
EDX	Energy dispersive x-ray spectroscopy
ETD	Everhart-Thornley detector
FFT	Fast Fourier transform
GIXRD	Grazing incidence x-ray diffraction
GOX	Gate oxide
GPC	Growth per cycle
HAR	High aspect ratio
HEMT	High-electron-mobility transistor
HRTEM	High-resolution transmission electron microscopy
HV	High vacuum
IC	Integrated circuit
LED	Light-emitting diode

MEMS	Micro-electro-mechanical system
MOCVD	Metal-organic chemical vapor deposition
NBED	Nanobeam electron diffraction
PEALD	Plasma-enhanced atomic layer deposition
PECVD	Plasma-enhanced chemical vapor deposition
PVD	Physical vapor deposition
SAED	Select area electron diffraction
SE	Secondary electrons
SOI	Silicon on insulator
STEM	Scanning transmission electron microscopy
TEM	Transmission electron microscopy
TMA	Trimethylaluminum
ToF-ERDA	Time-of-flight elastic recoil detection analysis
WDX	Wavelength dispersive x-ray spectroscopy
WPOA	Weak-phase object approximation
XRD	X-ray diffraction
XRR	X-ray reflectivity

d	Thickness
I	Intensity
p	Pressure
R	The gas constant
T	Temperature
V	Crystal potential

γ	Surface free energy
ΔG	Change in Gibbs free energy
λ	Wavelength
σ	Interaction constant
Ψ	Electron wavefunction
ω	Angle between a surface and the incident beam

List of Publications

This doctoral dissertation consists of an overview of the following publications, which are referred to in the text by their Roman numerals.

I Broas, M., Sippola, P., Sajavaara, T., Vuorinen, V., Pyymaki Perros, A., Lipsanen, H., Paulasto-Kröckel, M., "Structural and chemical analysis of annealed plasma-enhanced atomic layer deposition aluminum nitride films," Journal of Vacuum Science & Technology A: Vacuum, Surfaces, and Films, 34, (2016), p. 041506.

II Broas, M., Kanninen, O., Vuorinen, V., Tilli, M., Paulasto-Kröckel, M., "Chemically stable atomic-layer-deposited Al2O3 films for processability," ACS Omega, 2, (2017), pp. 3390-3398.

III Broas, M., Jiang, H., Graff, A., Sajavaara, T., Vuorinen, V., Paulasto-Kröckel, M., "Blistering mechanisms of atomic-layer-deposited AlN and Al2O3 films," Applied Physics Letters, 111, (2017), p. 141606.

IV Rontu, V., Sippola, P., Broas, M., Ross, G., Sajavaara, T., Lipsanen, H., Paulasto-Kröckel, M., Franssila, S., "Atomic layer deposition of AlN from AlCl3 using NH3 and Ar/NH3 plasma," Journal of Vacuum Science & Technology A: Vacuum, Surfaces, and Films, 36, (2018), p. 021508.

V Broas, M., Lemettinen, J., Sajavaara, T., Tilli, M., Vuorinen, V., Suihkonen, S., Paulasto-Kröckel, M., "In-situ annealing characterization of atomic-layer-deposited Al2O3 in N2, H2, and vacuum atmospheres," Submitted.

Author's Contribution

Publication I:

The author collaborated equally with M.Sc. Perttu Sippola. The author planned and conducted the annealing experiments and a considerable part of the characterization (ellipsometry, XRR, XRD, FTIR, TEM), and assisted in the atomic layer deposition. Dr. Graff and Dr. Poppitz assisted the author in transmission electron microscopy. The results and their interpretation were discussed with Mr. Sippola and the other stakeholders. The author wrote 50% of the manuscript and was the main correspondent during the review process.

Publications II, III, V:

The author planned the experimental work based on discussions with the stakeholders. The experimental work and analysis were mainly conducted by the author with the help from research assistants and colleagues who were instructed by the author. More specifically, the author himself conducted annealing experiments in the vacuum oven, characterization via ellipsometry, electron microscopy with SEM and TEM, sample preparation with FIB, XRR, XRD, and optical microscopy. The results and their interpretation were discussed with the co-authors. The manuscripts were written by the author and the conclusions were drawn by the author.

Publication IV:

The author initiated the research and planned it in close collaboration with the main author and the other co-authors. The author conducted a part of the experimental research and analysis including atomic layer deposition and film characterization (ellipsometry, curvature measurements, XRD, TEM). The author assisted the co-authors in the result interpretation and writing the manuscript. The main part of the manuscript was written by M.Sc. Ville Rontu.

1. Introduction

The key enabler in enhancing the digital world for tens of years has been the ability to miniaturize electronic devices. The miniaturization process has been steadily following Moore's law where the number of transistors on a die of the same size doubles every 18 to 24 months [1]. Moore's law has worked well in multiplying the computing power modern computers provide but it has not provided means for a more diversified digital world. The smartphone provides a great example of a more diversified digital world. A smartphone is certainly not operating merely as a pocket computer or as a phone. A smartphone is also a camera, global navigation satellite system, gaming device, and so much more. They key driver behind this is the concept of More than Moore (Fig. 1.1) [2]. Both continued transistor scaling (More Moore) and device diversification (More than Moore) impose continuous challenges on the semiconductor industry: the increased demand of diversified functions requires additional innovation in design and manufacturing.

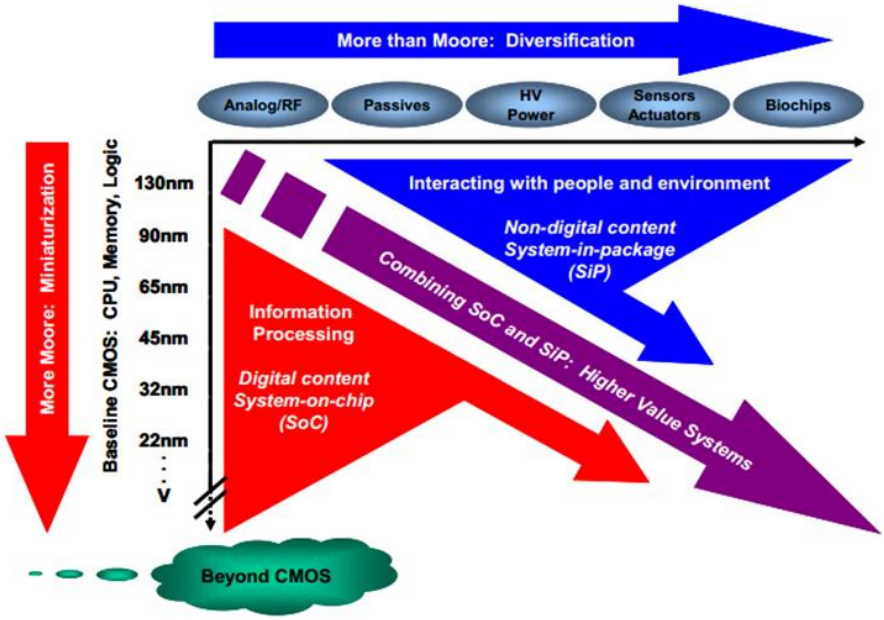


Figure 1.1. Transistor scaling combined with new technologies, such as miniaturized sensors, can produce more diverse, higher value systems. At the time of this dissertation the state of the art transistor node was around 10 nm. Adapted from [2].

New materials, new processing techniques, and the adaptation of already-developed materials are all required to meet the innovation challenges faced when extending Moore's law and developing more diverse applications. Perhaps one of the best-known examples of a recent paradigm shift in semiconductor processing was when the state of the art complementary metal-oxide-semiconductor (CMOS) gate processing and materials changed from a thermally grown SiO_2 gate oxide (GOX) and a polysilicon gate metal to an atomic-layer-deposited (ALD) HfO_2-based stack GOX and a metal-based gate. A major reason for selecting ALD was its ability to control the film thickness down to individual atomic layers, conformality on high aspect ratio (HAR) structures, and uniformity over large diameter wafers. The same properties of ALD can also be exploited in sensor and actuator applications for the functional diversification. Micro-electro-mechanical systems (MEMS) often have complex three-dimensional shapes which require conformality only provided by ALD. In addition, applications such as biochips can require protective, biocompatible coatings that need to be fully conformal. Outside of microelectronics, ALD coatings can be used as barrier layers against moisture and corrosion in applications where irregular surfaces need to be covered.

A bit over 40 years since its discovery, ALD films are found in many applications [3]. However, other deposition techniques may have trumped ALD in terms of film quality in the older technology nodes and at a time of less diverse selection of integrated devices. However, ALD has become increasingly more attractive as the new transistor nodes require thickness control in the order of single atomic layers, transistors have become three-dimensional (fin field effect transistor, FinFET) [4], and sensors [5,6] and semiconductor packages [7,8] have complex HAR structures. Therefore, more efforts are needed to come up with new ALD materials and to engineer the already-developed ALD materials to be suitable in new applications. The thin film engineer needs to work in close collaboration with the designers and process engineers to understand the complete process flow and the final requirements of the film. A film deposited at the beginning of the process flow may see elevated temperatures and harsh chemicals which may modify the film's microstructure, stoichiometry, the presence of impurities, film interface structure, film total thickness, and stress state. A film deposited at the end of the processing, such as a barrier film, needs to be robust with respect to the intended use of the application and its lifetime. Furthermore, if the protective film is deposited on a moving sensor element, its properties, such as residual stress, need to be thoroughly understood and modifiable.

This dissertation aims to reconcile the deposition of high-quality ALD AlN and Al_2O_3 films and their thermal treatment to simultaneously further refine their microstructure and to study their high-temperature stability. The films are investigated for their quality and from the perspective of stability in demanding environments, which can either be the environment during processing or the in-use environment. The intended use of the both films include applications in microelectronics such as silicon on insulator (SOI) buried dielectric layer (AlN and Al_2O_3) and barrier layer for corrosion protection (Al_2O_3). SOI-based integrated

circuits (IC) could benefit from replacing the current dielectric, SiO_2, with a dielectric layer of better thermal conductivity and on-par dielectric properties. The better thermal conductivity of the buried dielectric would alleviate transistor self-heating, which causes degradation of many transistor parameters and presents reliability concerns [9]. An Al_2O_3-based SOI, on the other hand, would enhance HAR micromachining of MEMS as the etch stop capability of alumina, in terms of the etch rate of the mask, is orders of magnitude lower than that of SiO_2 [10,11]. Finally, for similar reasons as for the HAR etch stop capability, i.e. chemical and physical robustness, alumina can be utilized as a protective layer against wear and corrosion. Both materials are well characterized in their bulk form, while as ALD films their thermal and chemical stability are not well understood.

The research questions were divided into three aspects:

i) Finding suitable process parameters for the deposition of high-quality ALD AlN and Al_2O_3 films. [**I**], [**II**], [**IV**]
ii) Exposing the films to thermal treatments to understand their thermal stability and to refine their microstructure. [**I**]–[**III**], [**V**]
iii) Using microstructure refinement to make the films chemically and thermally stable. [**II**], [**V**]

The contents of this dissertation are arranged in the following way. First, the term “film quality” and its dependency on the processing conditions are defined in Chapter 2. Chapter 3 discusses the fundamentals of atomic layer deposition and the relevant film quality aspects from the perspective of AlN and Al_2O_3. Chapter 4 details the characterization methods utilized in this work and shows practical examples of the type of information that can be obtained from thin films. In Chapter 5, the thermal and chemical stability are discussed and how one can affect them by selecting the appropriate annealing conditions to refine the film microstructure. Finally, in Chapter 6, the prospects of the achieved results are demonstrated and discussed to lay the groundwork for applying the results in further engineering work.

2. Thin Film Processing–Quality Relationships

Thin film deposition methods for microelectronics can be roughly divided into three categories: chemical vapor deposition (CVD), physical vapor deposition (PVD), and liquid phase deposition methods.[12,13] Vacuum-based CVD and PVD methods are suitable for the accurate process control demanded when depositing films in the thickness range of 10–1000 nm, while liquid phase deposition methods, such as electroplating, become more feasible in the film thickness range of microns.[13] This thesis focused on the deposition of films in the range of tens of nanometers and the liquid phase deposition methods are not discussed in the following text. The process–quality relationships are also different for the three categories of deposition methods as the physics are different. PVD is based on particles being physical ejected from a target and landing on a substrate, CVD on chemical reactions of vapors that take place at the substrate, and liquid deposition methods on a variety of mechanism in which the film precursor is in the liquid form. Since ALD is a subset of CVD, this chapter briefly discusses the processing–quality relationships of thin films mainly from the perspective of CVD type methods.

All CVD methods include similar reactions that take place as highlighted in Figure 2.1. The decomposition and subsequent reactions of the source gas are achieved either via thermal activation, via plasma-assisted reactions in plasma-enhanced CVD (PECVD), or through photon activation and the combination of thereof. Likewise, ALD can also be thermally activated, plasma-enhanced (PEALD), or photo-assisted [14]. An activation energy is required to be overcome to start the chemical reactions of the reactants (source gases) which will form the products (thin film) on the wafer. The change in the Gibbs free energy of the forming film is negative, i.e., the free energy of the film is less than that of the reactants, therefore making the film stable in the deposition conditions.

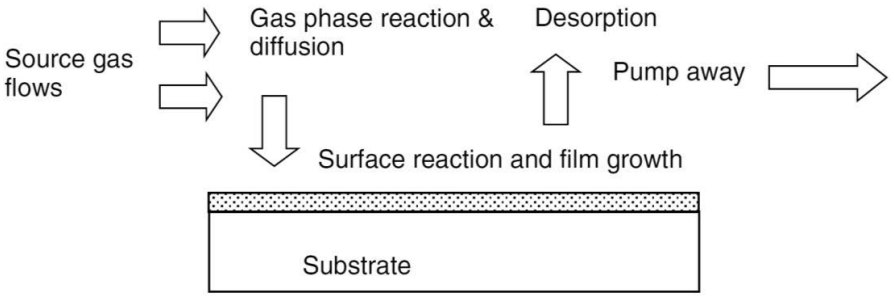


Figure 2.1 The principle of thin film growth via CVD methods. Figure is from [13].

The forming film can manifest various solid phases, such as different crystalline transition phases, a distorted stoichiometry, and the byproducts of the reaction may get trapped in the film. The resulting microstructure including the crystallinity, phase, defects as well as the trapped impurities in the film depend on the deposition conditions. For example, higher deposition temperature means that larger activation energies can be overcome to drive the reactions to the most stable phase of the film and the reaction byproducts can desorb more efficiently [15]. In other words, a higher activation energy means that a reaction depends more on the deposition temperature. Consequently, the kinetics of a higher activation energy process are slow at a lower deposition temperature meaning that reactions with a low activation energy, and less dependency on temperature, are favored. However, a higher temperature may also cause self-decomposition of one of the reaction gases causing unwanted impurities to get embedded in the film [16].

Furthermore, since the coefficients of thermal expansion (CTE) typically differ between the substrate and the film, there will be residual stress in the film at room temperature [17]. For example, an ALD alumina thin film on Si ($CTE_{Al_2O_3} > CTE_{Si}$) is in tensile stress at room temperature [18]. The alumina film strives to shrink more than the Si substrate as the film-substrate stack is cooled down to room temperature. The thick Si substrate restricts the shrinking alumina thin film causing tensile stress in the film. However, the CTE mismatch may not fully explain the film stress. For example, in [18] the ALD Al_2O_3 films deposited at lower temperatures had higher biaxial tensile stresses at room temperature than the films deposited at higher temperatures. Other effects, such as cluster coalescence, have to take place during the film growth to induce additional stresses [19,20]. High stresses in films can cause defects such as cracking and delamination. Therefore, the deposition temperature needs to be optimized from the perspective of stress.

The growth mechanism also affects the quality of the forming film. The activation energy is modified if the film growth takes place on a surface with reactive sites, such as OH groups in the case of trimethylaluminum-based deposition, or on a template and epitaxial or substrate-assisted growth takes place [21]. An additional stress component can arise from the lattice mismatch of the growing film and the substrate in the case of heteroepitaxy [22]. The larger the lattice mismatch,

the more defects, such as dislocations, are needed to accommodate the epitaxial growth.

A third mechanism for additional stresses in thin films is related to the plasma-activation: the high-energy ions may collide with the substrate and the growing film causing collision cascades and densification of the film and thus modify the stress state of the film [23]. Post deposition thermal treatments can be utilized to alter the film quality by inducing crystallization, degassing of unstable byproducts that were embedded in the film, and modifying the stress state.

In summary, the processing–quality relationships are an interplay between the deposition activation mechanism (temperature, plasma), source gases including the atmosphere (product vs. reactants free energy, self-decomposition), and substrate (growth mechanism, substrate vs. film CTE). It should be noted that the term "quality" can be understood in many ways within the context of depositing thin films. In addition to the previously discussed impurities, film phase (crystallinity), stoichiometry, and stress, other important processing–quality-relationships, such as uniformity, thickness control, interface abruptness and structure, conformality, and deposition selectivity should not be neglected [15].

The adequate quality of a thin film also depends on the purpose. For example, an optical coating in a hermetic package will see a very different environment and further process steps compared to an etch stop layer or a CMOS gate dielectric. The following chapters will discuss such processing–quality relationships, the effect of additional thermal treatments on the film quality, suitable characterization methods for characterizing the film quality, and the impact of the film quality on its microstructural stability during thermal and chemical solvent treatments. Most notably, transmission electron microscopy (TEM) was utilized heavily in studying the microstructure-related aspects, such as crystallinity, grain orientation, interfaces, and their development from as-deposited to annealed films.

3. Atomic Layer Deposition

Atomic layer deposition was used in this thesis to deposit AlN and Al_2O_3 films. This chapter covers the principle of ALD and processing–quality relationships mainly from the perspective of stoichiometry, impurities, and microstructure. AlN and Al_2O_3 from Publications [**I**], [**II**], and [**IV**] are compared to the literature and other ALD films.

3.1 Principle, Stoichiometry and Impurities

The desired thin films are typically grown from two precursors in ALD. Both precursors are self-terminating in the ideal case. For example, an organometallic precursor reacts with the substrate via one of the ligands detaching and the organometallic attaching to a reactive site at the substrate. The detached ligands are flushed out during a purge cycle. After the purge cycle the second precursor is introduced. The second precursor can be for example water vapor in the case of oxide films and ammonia in the case of nitride films. The remaining ligands from the first cycle, still attached to the core of the first precursor, react with the second precursor and detach while the core of the second precursor reacts with the first core forming a monolayer of the desired film. The reacted ligands are flushed out subsequently. These cycles are repeated until the desired thickness is reached (Fig. 3.1).

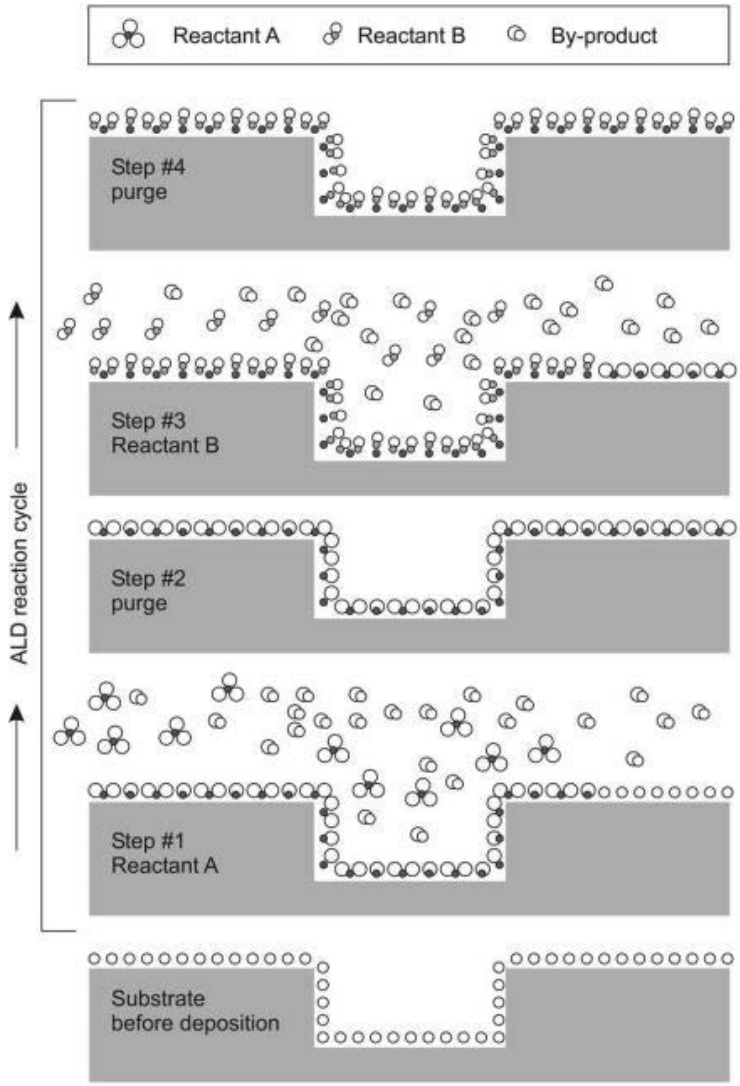


Figure 3.1. The ideal ALD cycle where one monolayer of the desired film is produced on the substrate. The surface is covered with ligands or simple atoms, for example hydrogen atoms, from the reactant B which serve again as reactive sites for the next cycle. Adapted from [24].

The ideal ALD process is in practice rarely reached. This means that various impurities may get embedded in the films via various reaction routes:

- Precursor ligand related (for example carbohydrates when using organometallics)
- Second precursor related (for example hydrogen from ammonia)
- Excess precursor core atoms distorting the stoichiometry

The embedded impurities and poor stoichiometry can result in inferior material properties and poor thermal and chemical stability of the films and are typically undesired. The suitable number of precursors is vast. Ritala et al. [25] list the following attributes as 'must' requirements:

- Sufficient volatility
- Aggressive and complete reactions
- Thermal stability (no self-decomposition)
- No etching of the film or substrate material
- No dissolution into the film substrate
- Sufficient purity

A good idea of the vast number of different precursors that have been studied can be obtained from the review by Miikkulainen et al. [26]. Although the review is more concerned with the crystallinity of ALD films, it is still possible to deduct something about the role of impurities in ALD films. The amount of impurities and the film crystallinity are likely linked as more complete precursor reactions, i.e., energetically favorable and thus crystallization promoting reactions, can lead to less impurities in films. For example, V_2O_5 from vanadyl-tri-iso-propoxide and H_2O at 150 °C by PEALD produced amorphous films with 22 at.% C, whereas impurity-free, crystalline films were produced with O_2 plasma [27]. However, sometimes simply observing the crystallinity of the film is not enough to make statements about the impurities. For example, in one study TiN grown from $TiCl_4$ was crystalline despite having 7.7 at.% Cl and 16 at.% H [26]. It is expected though that different impurities affect the phase stabilities differently [21].

The two most straightforward routes to decrease the amount of impurities are to select a suitable combination of precursors and to increase the deposition temperature. In addition, plasma-enhancement may be viable in decreasing impurities in the film and engineering the stoichiometry. However, the main function of using plasma-enhanced growth, whether being ALD or some other gas phase deposition, has been typically to lower the deposition temperature. The effects of plasma-enhanced growth are not always straightforward to interpret and secondary effects, coming for example from ion peening, can cause unexpected results [23]. Finally, the self-limiting growth of ALD requires a uniform and adequate dose of the reactants over the entire substrate. Hence, looking at the partial pressures of species inside the chamber may not have been as great of an interest as achieving the saturated growth behavior. Therefore, the saturated growth may have occurred in a situation where the ideal stoichiometry is not favored. On the other hand, it could potentially be possible to minimize certain impurities by depositing films with partial pressures that would well exceed the required dose but would inhibit impurities from embedding into the films.

3.2 ALD Aluminum Nitride

ALD AlN films can be deposited by a thermally-activated or plasma-enhanced process. The most typical precursor for Al is trimethylaluminum (TMA) whereas nitrogen can be introduced from either ammonia, ammonia plasma, or N_2/H_2

plasma. The impurities coming from the precursor gases are hydrogen, carbon, and excess nitrogen or aluminum distorting the stoichiometry. Carbon and oxygen may be introduced from the atmosphere due to poor isolation of the reaction chamber. TMA-based deposition is usually carried out below 400 °C due to the decomposition of the precursor [28]. The process can work above 400 °C also but the amount of carbon impurities may increase. Nevertheless, high crystalline quality AlN has been deposited at 500 °C with a TMA-based process [29]. These films had 4 at.% C and also rather high 3 at.% O content. Hydrogen was not measured in the study. Hydrogen is not often directly measured due to the limited availability of tools capable of quantitatively measuring hydrogen. Time-of-flight elastic recoil detection analysis is usually employed when also hydrogen is measured. The amount of hydrogen has been reported to be 13–27 at.% in PEALD processes utilizing TMA [30] [**I**]. The amount of hydrogen decreases with increasing the deposition temperature. When the isolation of the reaction chamber is good oxygen impurities are reported to be below 1 at.% although some carbon impurities in the range of 1 at.% are still expected when utilizing TMA [31]. Stoichiometry of the TMA-based PEALD AlN films has been reported to be both Al and N-rich with about 1.1 Al-to-N ratio being the closest to the ideal stoichiometry [32].

Lower hydrogen concentrations have been reported for thermal and plasma processes, when using $AlCl_3$ as the Al precursor, being 2 and 9 at.%, respectively [33,34]. In [**IV**] 6.5 at.% of hydrogen was achieved using $AlCl_3$ in the PEALD setup while a thermal process resulted in 10.9 at.% of hydrogen. The second reaction gas has been one containing hydrogen nevertheless. However, the films in [33,34] still contained Cl – 2 at.% in the plasma process and 9 at.% in the thermal process, while in [**IV**] 0.1 at.% Cl was achieved with the PEALD process and 3.8 at.% in the thermal ALD. The differences may arise from the chamber setup, gas partial pressures, and different hydrogen analysis methods.

In [**I**] and [**IV**] AlN was deposited from two precursor combinations: TMA-N_2/H_2 plasma and $AlCl_3$-NH_3 (both thermal and plasma processes were developed). The TMA process was conducted at 200 °C while the $AlCl_3$-based processes took place at 475 °C and 425 °C for the thermal and plasma process, respectively.

The TMA-based process was conducted with two N_2:H_2 ratios – 1:1 and 3:1. The growth per cycles (GPC) were both 0.06 nm/cycle. The thickness non-uniformities of the films were 1–2%. The precursor doses were considered saturated as similar GPCs had been reported in the literature [31,32,35,36] and the non-uniformities were low for a plasma process. On the other hand, the refractive indices at the wavelength of 632.8 nm were below 1.90 which can be considered rather low for AlN as the bulk value is roughly 2.10 [37] and values close to 2.0 have been reported for ALD AlN [38]. As the refractive index is mainly based on the density and polarizability of the material [39] it can be considered a good estimate for the quality of AlN. Furthermore, the AlN films were deemed unstable with respect to the amount of outgassing species and development of the microstructure during high vacuum (HV) annealing presented below in Section 5.2.

The $AlCl_3$-based process was first developed as a thermally-activated one at 475 °C [**IV**]. Figure 3.2 presents the thermal ALD dose saturation graphs. The solid $AlCl_3$ precursor container temperature was first optimized with a constant 4-s NH_3 pulse (Fig. 3.2a). A 1.5-s pulse was used for $AlCl_3$ with a boosting function where the gaseous precursor coming from the solid source was collected in advance and then flushed into the chamber. The GPC and the refractive index of the optimized process were 0.07–0.08 nm and 1.93.

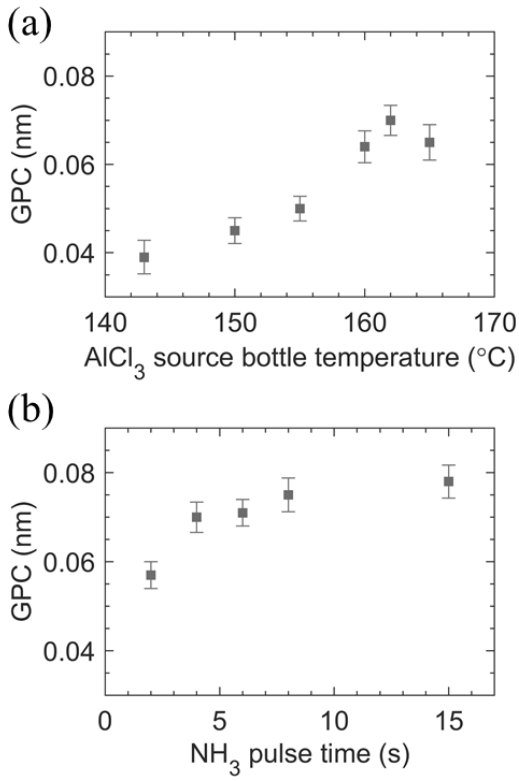


Figure 3.2. Dose saturation graphs for the thermal AlN process. The optimized process was run with 6-s NH_3 pulsing at the $AlCl_3$ bottle temperature of 162 °C. The $AlCl_3$ temperature optimization was conducted with the NH_3 pulse being 4 s (i.e. the data points lying at 0.07 nm GPC in (a) and (b) correspond to the same deposition run). [**IV**]

The PEALD process was based on the $AlCl_3$ temperature and pulse time (162 °C and 1.5 s with the boosting function). The NH_3(Ar) plasma time was varied and was also used in a configuration where an additional NH_3 pulse without the radio frequency power was introduced between the $AlCl_3$ and the plasma pulses (Plasma ABC in Fig. 3.3). The GPCs and refractive indices were approximately 0.03–0.04 nm and 1.9–2.0 for both plasma processes. However, the AB plasma process induced a high compressive stress into the films which caused blistering [**III**]. Therefore, the ABC process was used to decrease the compressive biaxial stress in the films. The biaxial stresses were measured with the wafer curvature method by applying the Stoney's equation [17]. The $AlCl_3$-based films were not an-

nealed to further improve the quality in terms of impurities and grain size. Annealing in ultra-high vacuum conditions or in forming gas to prevent oxidation could be applied to further refine the AlN films.

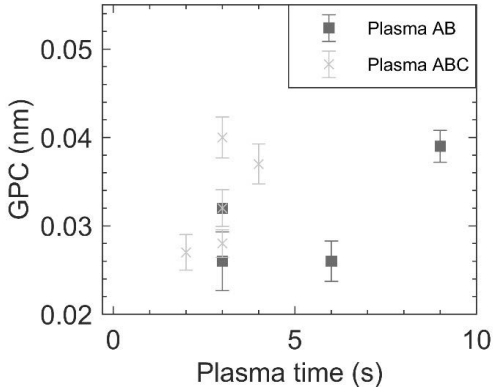


Figure 3.3. GPC as a function of the plasma time. AB refers to a binary process of $AlCl_3$-NH_3(Ar) plasma and ABC to a process with an $AlCl_3$-thermal NH_3-NH_3(Ar) plasma sequence. [**IV**]

3.3 ALD Aluminum Oxide

Alumina is typically grown from TMA or $AlCl_3$ and water vapor.[24,26] Also, for example ozone can be used as the oxygen source. Growth temperatures between below 100 °C and 500 °C have been typically reported although limited studies exist on higher temperature deposition too.[26,40] The upper limit of 500 °C tends to come from the fact that it is the maximum temperature for which ALD reactors have been designed. The precursor decomposition temperature must be considered also when developing the process. The ALD alumina deposition is well established and the films have been reported to have a low amount of impurities. The lower temperature regime films contain more hydrogen, whereas high-temperature films grown with TMA may contain some carbon. The amount of hydrogen can be driven very low in both TMA and $AlCl_3$ processes. At a moderate deposition temperature of 250 °C from TMA 1 at.% of hydrogen has been reported [41], and at a very low temperature of 33 °C the H concentration has been reported to be 22 at.% [42]. In [41] the carbon content of the film was < 0.3 at.%. It is obvious that despite the metal precursor being the same in both AlN and Al_2O_3 the latter one has more explosive reactions (larger driving force) leading to more complete reactions.

In [**II**] ALD Al_2O_3 was deposited from TMA, $AlCl_3$, H_2O, and O_3 at different temperatures. The films that were deposited at 450 °C from TMA and H_2O were finally investigated the most thoroughly since their GPC of 0.07 nm, refractive index of 1.66, and non-uniformity of 1% were adequate for further processing and applications. The process development was carried out at Beneq Oy and is not presented here. It is worth mentioning though that the same ALD alumina recipe is used to deposit an ion barrier for electroluminescence displays. The 450 °C TMA-H_2O-based films contained 0.21 at.% hydrogen and 0.07 at.% car-

bon. The small amount of carbon is rather surprising as TMA starts to self-decompose at 370 °C [43,44]. However, the degree of adverse effects coming from the self-decomposition can be minimized with the correct reactor design and deposition parameters.

3.4 Microstructure

A thorough overview of the crystallinity of ALD films is given in [26]. In summary, many types of microstructures are observed in as-deposited ALD films: amorphous [**II**], nanocrystalline [**IV**], polycrystalline [45], and even epitaxial [29]. Obviously, the deposition temperature plays a dominant role together with the precursors in which phase is manifested in the as-deposited state. However, some generalizations can be made. For example, typical ALD temperatures result in an amorphous structure for the thermal process of Al_2O_3 (Fig. 4.6) while crystalline HfO_2, TiN, and TiO_2 can be achieved in thermal ALD routinely at the sufficient temperature of each specific process (Fig. 3.4).

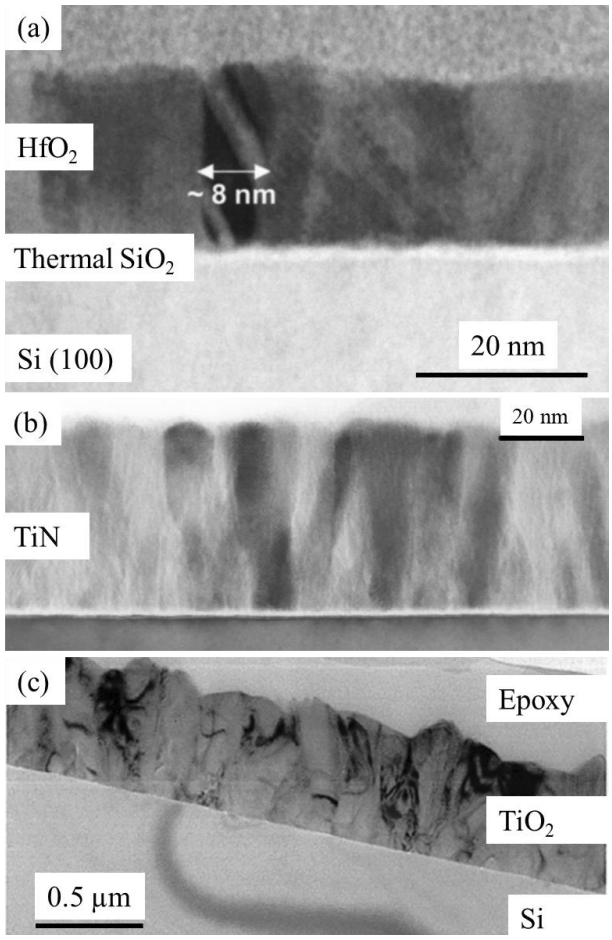


Figure 3.4. As-deposited crystalline ALD films. HfO_2 [46] (a) and TiN [47] (b) showing columnar grains while TiO_2 [45] (c) is showing random polycrystalline growth. The images are adapted from their respective references.

In [**IV**] the as-deposited AlN films showed a varying degree of crystallinity (Figure 3.5). The PEALD-based films exhibited similar columnar growth as the ones in Figures 3.4 (a) and (b). In the case of AlN, the hexagonal c-axis direction dominated the growth. A thin amorphous layer was visible between the films and the substrates in Figure 3.5 because the films were grown on SiO_2. However, the interfacial layer measures too thick to be only SiO_2 implying that the first deposited AlN layers are amorphous and crystalline AlN nucleates later during the deposition.

Contrary to ALD AlN, the as-deposited Al_2O_3 films are typically amorphous but crystallization can be achieved with annealing.[26,48] Figure 3.6 presents the TMA-H_2O-based film from [**II**] that was annealed at 1000 °C in a flowing nitrogen atmosphere. The film crystallized in the θ phase with the $\{20\bar{1}\}$ planes preferentially stacked on the Si (100) substrate. Furthermore, an interfacial layer formed between the Si substrate and the alumina film which was identified to be composed of Si, O, and Al. Similar interfacial layer has been observed in References [49–52] too. An interfacial layer is also formed between HfO_2 and Si during processing from a combination of oxidation during deposition from the oxygen-containing precursor and the subsequent high-temperature processes [53]. The thickness of the interfacial layer can be decreased by depositing oxygen gettering materials on top of the HfO_2 which will attract oxygen during the high-temperature process steps. Furthermore, the formation and thickness of such interfacial layers, whether in Si-Al_2O_3 or Si-HfO_2, is governed by the stoichiometry of the deposited material (additional oxygen) and the thermodynamic equilibrium between the two dissimilar materials.

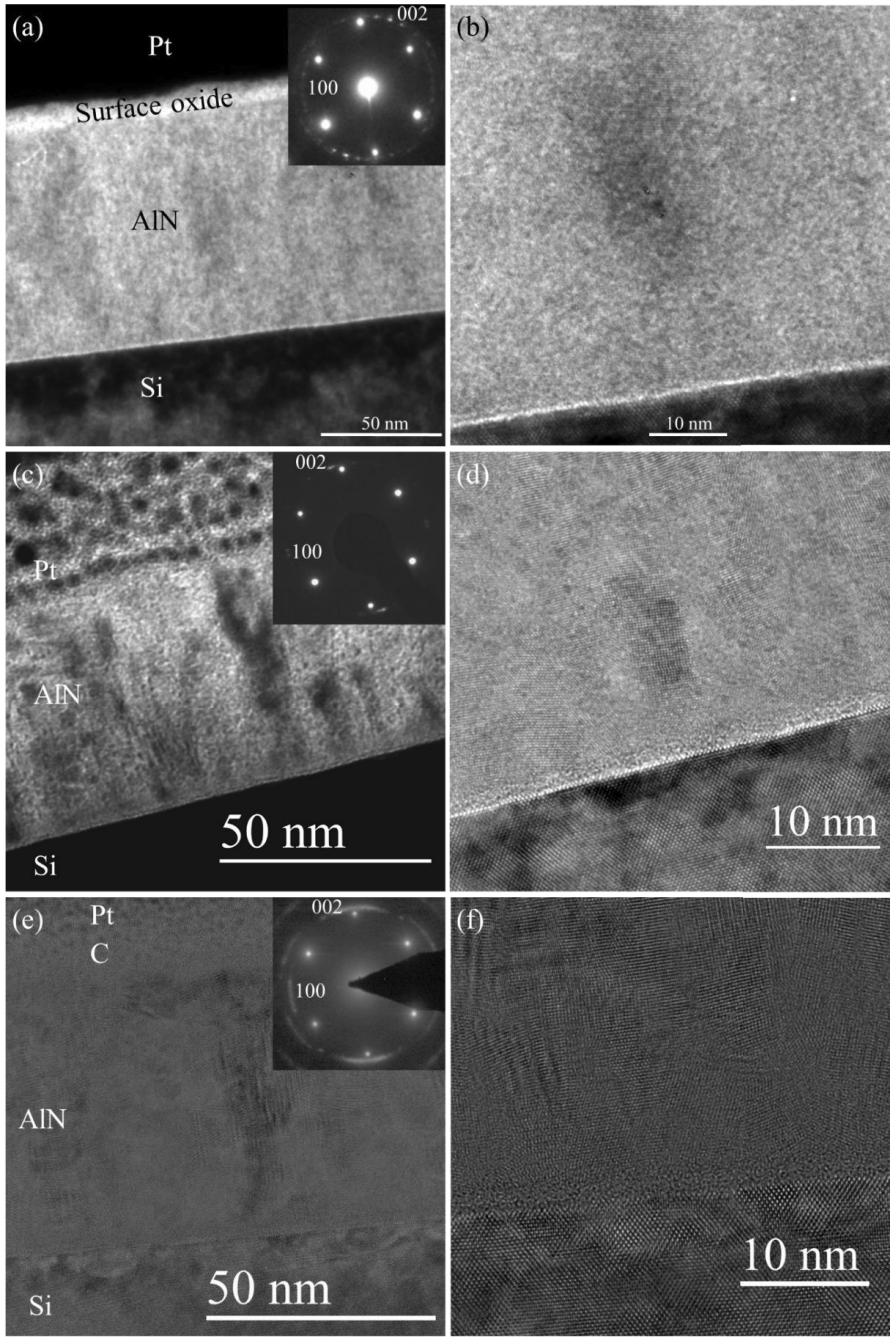


Figure 3.5. TEM images of the thermal and PEALD AlN films. The overview TEM images on the left were recorded with a small objective lens aperture (high diffraction contrast) and show partly crystalline structures. The high-resolution images on the right display the Si-AlN interfaces and lattice fringes in AlN corresponding to small crystallites. (a)-(b) Thermal $AlCl_3$-based AlN. (c)-(d) PEALD $AlCl_3$-based AlN deposited via the ABC 3 s process. (e)-(f) PEALD $AlCl_3$-based AlN deposited via the AB 6 s process. The electron diffraction patterns were recorded along the Si <110> zone axis. The indices correspond to w-AlN. The bright, unindexed spots are Si reflections.

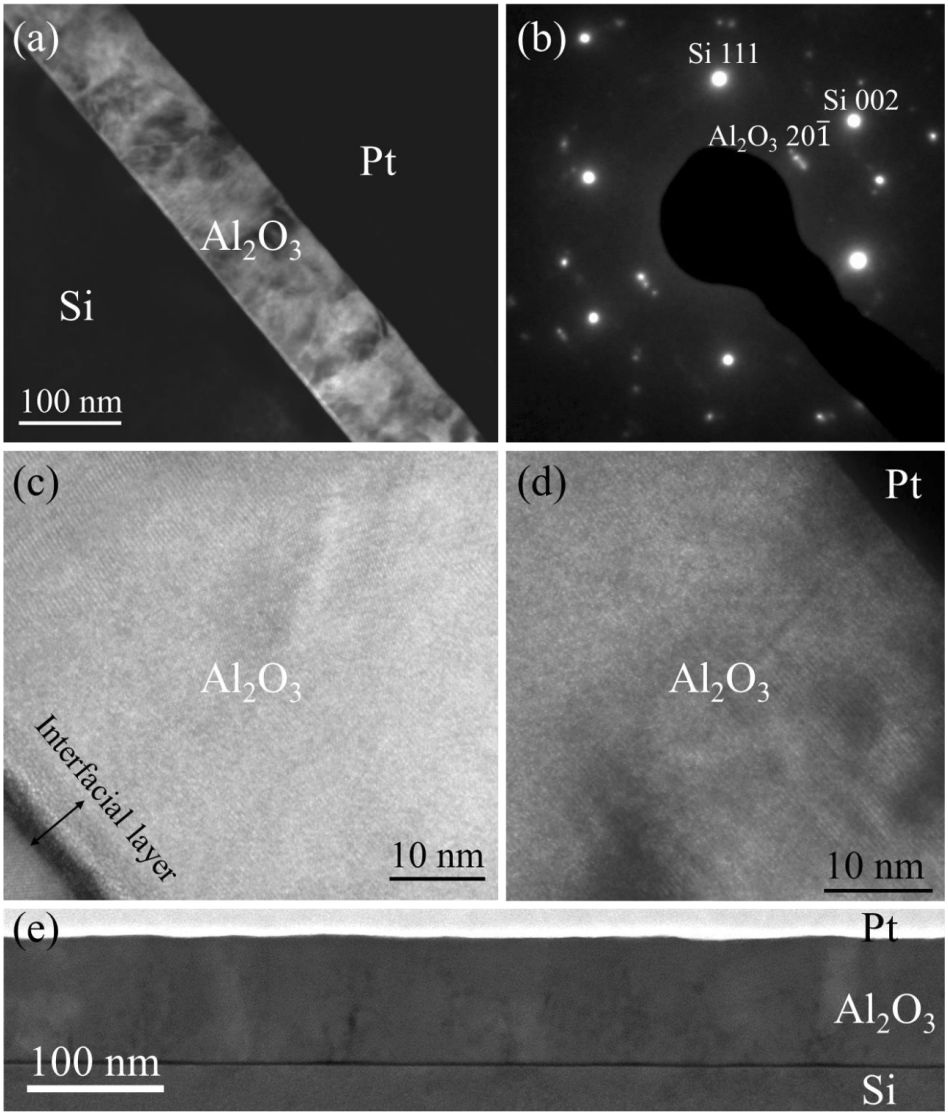


Figure 3.6. TEM images of ALD Al_2O_3 annealed in N_2 at 1000 °C. (a) An overview bright-field image shows a polycrystalline structure. (b) The select area electron diffraction aperture was used to select Si and Al_2O_3 and the lamella was oriented according to the Si <1$\bar{1}$0> zone axis showing a preferential orientation for the crystallized alumina with θ-alumina (20$\bar{1}$) planes along the Si [002] direction. High-resolution images of the Si-Al_2O_3 interface (c) and the Al_2O_3 surface (d). (e) A dark-field scanning TEM image shows that the alumina film has crystallized uniformly.

4. Structural and Chemical Characterization Methods of Thin Films

The structural and chemical characterization methods of thin films probe the crystal structure, microstructure, and composition of the films. The surface and the substrate-film interface comprise of a notable portion of the thin film thickness and need to be characterized thoroughly together with the film to understand the properties and behavior of the complete material system. This chapter discusses characterization methods which were used in the film characterization of this thesis. Theory is combined with actual images of different material systems to describe the type of information that can be obtained with the respective method. Many other methods exist also and the chapter is not meant to be an exhaustive list of all different thin film characterization methods.

4.1 Electron Microscopy

Electron microscopy is routinely applied in microelectronics research and manufacturing. Scanning electron microscopy (SEM) images are straightforward to produce with the modern systems and do not require extensive training to qualitatively understand the gray scale contrast of the produced images. It is nevertheless a versatile tool and different detectors collecting secondary electrons (SE) and back-scattered electrons (BSE) with different incident angles give information about the topography and mass density of the sample. There is no one-best-way to use an SEM as the produced contrast depends on the sample, the utilized detector, and electron beam parameters such as the acceleration voltage. However, as a rule of thumb the SE detectors, such as the Everhart-Thornley detector (ETD) and in-lens detectors best capture the topography of the sample, while dedicated BSE detectors are used to collect electrons emitted from deeper in the sample giving rise to the mass density contrast. Additionally, other detectors may be integrated into an SEM such as electron back-scatter diffraction (EBSD) for crystal structure analysis, and energy/wavelength dispersive x-ray spectrometers (EDX/WDX) for composition analysis. Figure 4.1 presents a schematic of an SEM column with different detector arrangements and the type of information that can be collected from a sample in a well-equipped SEM.

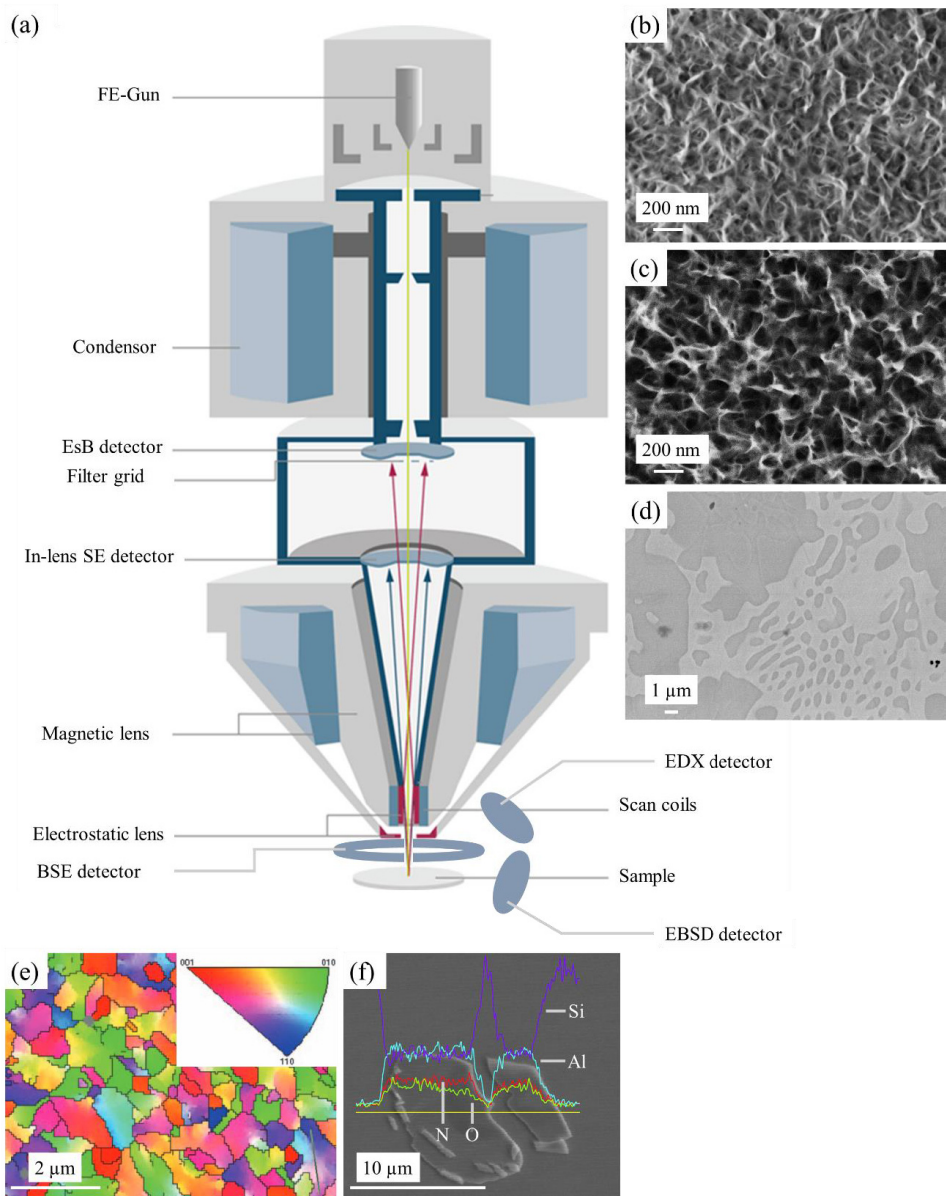


Figure 4.1. A schematic picture of an SEM column (a) and images collected with different detectors. Topography in-lens (b) and ETD (c) SE images of an ALD Al_2O_3 film that had corroded in water causing aluminum hydroxide growth **[II]**. (d) A BSE image of an AlAuCu alloy showing Z contrast information of two intermetallic compounds (Alloy 1 in [54]). (e) An EBSD inverse pole figure map of an ALD TiO_2 film in the anatase phase deposited on ALD Al_2O_3 [55]. (f) An SE image and EDX line profile (signal magnitude is in photon counts) of an ALD AlN flake on Si. The SEM column schematic is adapted from [56]. Figure (e) is adapted from [55].

As the physical dimensions in the microelectronics manufacturing have continued to shrink [57], the resolution of SEM and SEM-EDX have become insufficient. The much smaller de Broglie wavelength of electrons in transmission electron microscopy (TEM), operated typically at 200 or 300 kV, makes TEM superior compared to SEM in terms of resolution. The thin, electron-transparent

samples also emit x-rays for EDX analysis from a much smaller area compared to SEM-EDX where chemical information is obtained from a volume in the micrometer-order. In contrast, in scanning TEM (STEM) EDX the spatial area for chemical analysis is in the same order as the probe size – around 1–10 nm (Fig. 4.2).

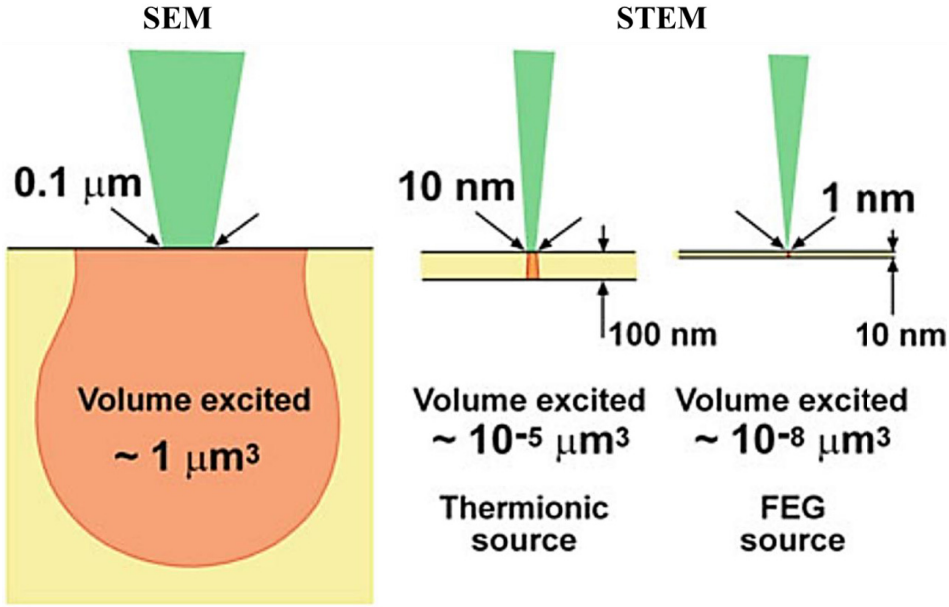


Figure 4.2. A comparison between the excitation volumes of characteristic x-rays in SEM and TEM systems. Adapted from [58].

However, the superiority of TEM compared to SEM also means that it is much more time consuming to operate and master. Furthermore, the sample preparation for TEM is not trivial and requires expensive tools such as focused ion beam systems. Nevertheless, Figure 4.3 presents a schematic of a TEM and examples of obtainable information. Note that the TEM system comprises of many lenses and apertures which are manipulated to produce the desired type of image.

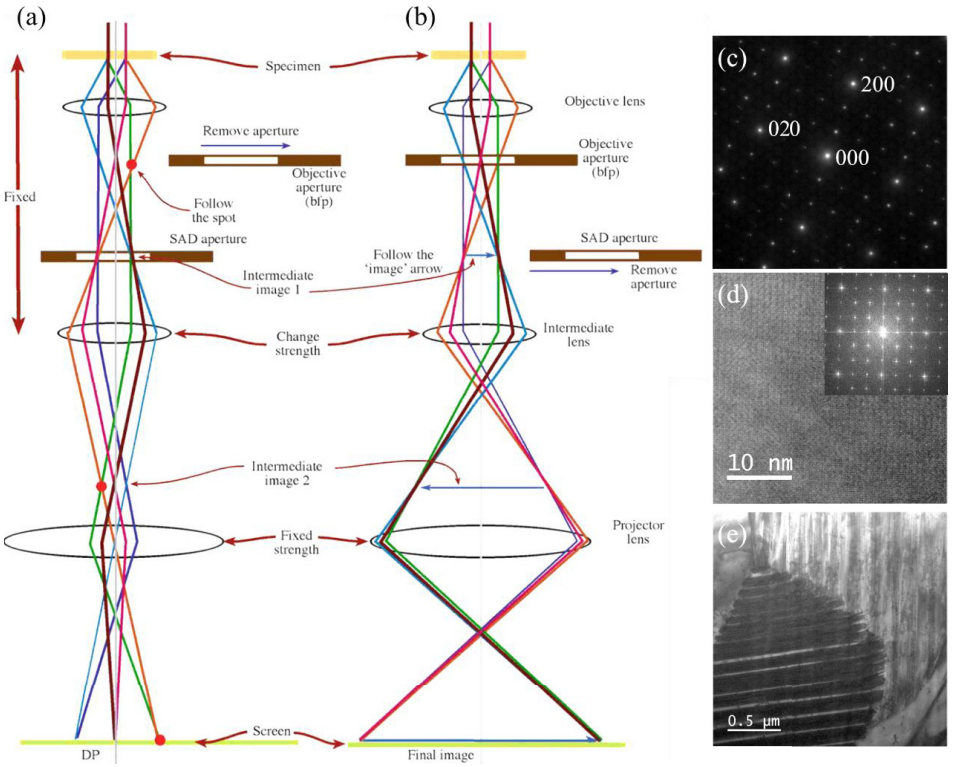


Figure 4.3. Schematics of TEM columns and example images with different imaging modes. The beam diagrams for obtaining diffraction patterns (a) and images (b) [58]. (c) A select area diffraction pattern of an AlAuCu-based superlattice structure [54]. (d) A high-resolution TEM image and the respective fast Fourier transform (FFT) image of the same alloy [54]. (e) A bright-field image of a similar AlAuCu alloy that has undergone the martensite transformation and shows twinning [54]. The beam diagrams are adapted from [58].

TEM techniques can be roughly divided into diffraction contrast imaging (Fig. 4.3e), electron diffraction (ED, Fig. 4.3c), phase-contrast imaging (Fig. 4.3d), and analytical TEM (Fig. 4.8 presented later). In analytical TEM the microscope is typically operated in the STEM mode where bright-field (BF) and dark-field (DF) imaging give more possibilities to produce contrast-rich images with different information of the sample under investigation. Just as with SEM, there are several options on what imaging mode to use and the 'correct' selection depends on the sample and the type of information that needs to be collected. However, unlike in SEM some of the imaging modes may require reproducing the images via simulations to truly understand the contrast differences of the image.

4.1.1 Electron Diffraction

Coherently scattered electrons are projected onto the screen/camera in the diffraction operation mode of TEM. The ED patterns give information about the structure of the sample. Most notably amorphous, polycrystalline, and single crystalline materials form either a halo, rings, or single bright dots, respectively,

onto the screen (Fig. 4.3 a and c). Furthermore, the ED pattern gives information about the symmetry and lattice spacing of the sample. Based on the symmetry and lattice spacing it is possible to deduct the orientation of the sample when the crystal structure is known, or to assign a correct crystalline phase to the material under investigation. When a thin film is deposited on a Si substrate, one can orient the interface between the substrate and the film to be perpendicular to the electron beam by rotating the sample with the help of the ED pattern of silicon. For example, on (100) Si substrates the desired perpendicular direction is usually the <110>. Figure 4.4 presents an example TEM image and the corresponding select area electron diffraction (SAED) pattern of a polycrystalline PEALD AlN with slightly preferentially oriented hexagonal c-axis perpendicular to the Si surface (100) substrate.

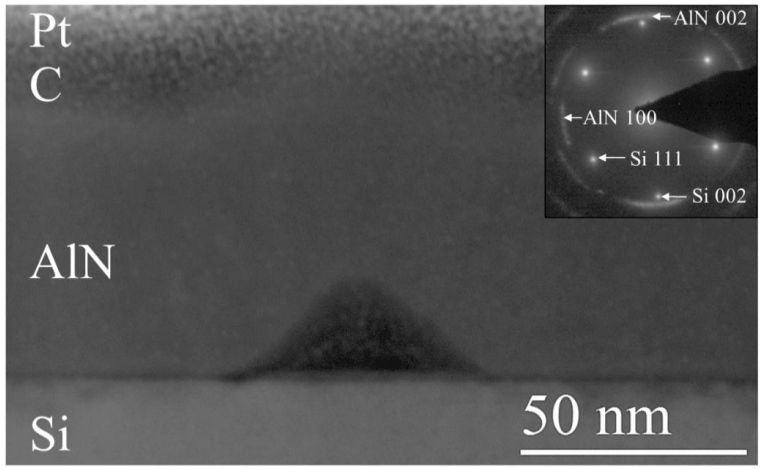


Figure 4.4. The lamella has been oriented according to the Si <1$\bar{1}$0> zone axis whose corresponding diffraction pattern is visible as the sharp dots in the SAED. The DF STEM image shows a polycrystalline structure. The indexed SAED pattern shows that the AlN crystallites are preferentially oriented with the hexagonal c-axis perpendicular to the surface of the Si substrate with some angular spread. The black area between AlN and Si is a defect (empty space) caused by wrinkling of the film due to a high compressive stress in the film [**III**].

In many cases it is useful to simulate the ED patterns by constructing the crystal with a software if the atom positions are known. The atom positions of many solids have been deducted with x-ray, neutron, and electron diffraction and such information can be found for example in the Inorganic Crystal Structure Database (ICSD) [59]. Figure 4.5 presents an example where a low-index zone axis was found by trial and error in a ternary AlAuCu metal system [54]. There was a good initial guess of the correct phase based on visual light microscopy, SEM, and chemical analysis data [54,60,61]. The system was constructed based on atomic position data from [60] where either a monoclinic or an orthorhombic unit cell were proposed. Based on the simulation, the monoclinic unit cell fit the experimental results better giving confidence on assigning the correct structure for the observed phase.

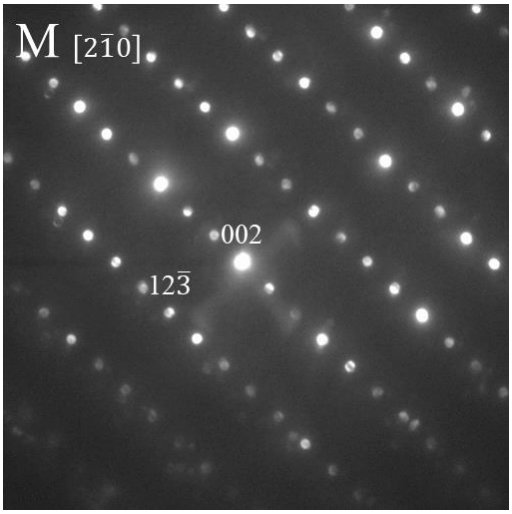


Figure 4.5. A ternary AlAuCu alloy that is known to have shape-memory properties was best indexed as the martensite-transformed monoclinic system after comparing the experimental pattern with simulations. The BF TEM image was presented in Fig. 4.3e. The SAED pattern was obtained from one of the twinned crystals by converging the beam slightly to capture the SAED pattern of only one grain.[54]

4.1.2 Diffraction Contrast Imaging

Diffraction contrast imaging is a generic name for TEM imaging where the contrast in the image mainly arises from the different parts of the sample diffracting the passing electron beam with different conditions. The collected electrons lie in the image plane, i.e., the obtained image is a magnification of the actual sample (Fig. 4.3 b and e). By tilting the sample, hence influencing the arising diffractions, and using the objective lens aperture to select desired reflections, one is able produce notable differences in contrast coming from the different parts of the sample. Diffraction contrast imaging is especially useful for imaging defects as the diffraction conditions are extremely sensitive to local deviations, such as dislocations and nanocracks, in the sample. The contrast may be further enhanced by tilting a crystalline sample into a two-beam condition, where only two strong beams are present (central and one diffracted). This will also give directional information about defects.

The imaging can be either BF or DF type. BF imaging simply means that the zero-order central beam is included in the image formation whereas in DF imaging the central beam is completely excluded. In this thesis, the most frequently used imaging condition for the diffraction contrast imaging was with selecting only the zero-order beam with a small objective lens aperture. This imaging condition highlights amorphous regions in the sample as those regions will not diffract the beam. An example of the zero-order beam imaging is in Figure 4.6. Many defects will be highlighted too. The contrast differences are further digitally enhanced using a digital software (Digital Micrograph® with Gatan cameras). Metals and other high Z number materials might require the user to let some of the diffracted beams to pass onto the charge-coupled device (CCD)

also since the intensity of the zero-order beam might be too low due to the material heavily incoherently scattering the beam. The incoherently scattered electrons are exploited in Z contrast imaging with STEM explained later.

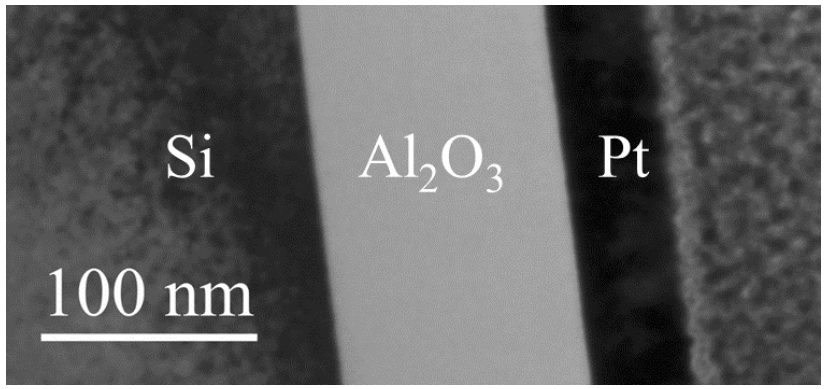


Figure 4.6. A BF image of as-deposited ALD Al_2O_3 where only the central zero-order beam was selected. The amorphous alumina scatters the beam little giving high, uniform intensity on the CCD. [**II**]

4.1.3 Phase-contrast Imaging

Phase-contrast imaging usually refers to high-resolution TEM (HRTEM) as phase-contrast is the dominant effect contributing to the HRTEM image formation. Contrary to the diffraction contrast imaging, more than one beam needs to be selected to achieve phase-contrast. The contrast is produced by changes in phases of the diffracted waves hence more than the zero-order beams needs to be selected.[62]

The crystal potential modifies the phase of an incident electron wave. The projected potential of a crystal in the z direction, *V(x.y)*, modifies the wave function Ψ of an electron after the sample:

$$\Psi(x,y) = e^{i\sigma * V(x,y)} \approx 1 - i\sigma * V(x,y) \tag{4.1}$$

where σ is the interaction constant. The 'almost equal to' part of Equation 4.1 is the weak-phase object approximation (WPOA) which assumes the specimen to be a weak scattering object, i.e., the specimen needs to be very thin with minimal absorption. To find the total intensity of a transmitted and diffracted beam:

$$I = \Psi\Psi^* = 1 + \sigma^2 V^2 \approx 1 \text{ since } \sigma^2 V^2 \ll 1 \tag{4.2}$$

That is, no contrast is produced on the CCD due to the interference of the transmitted and diffracted beams that have undergone a phase shift when exiting the sample. However, the objective lens is defocused to introduce a phase shift of $\pi/2$ in the diffracted beams:

$$I = \Psi\Psi^* = 1 - 2\sigma V + \sigma^2 V^2 \approx 1 - 2\sigma V \tag{4.3}$$

which means that the contrast at the CCD will be a linear function of the projected crystal potential.[63] Figure 4.7 presents two HRTEM images. To fully understand HRTEM images they need to be simulated to correctly position the atoms in the obtained image.

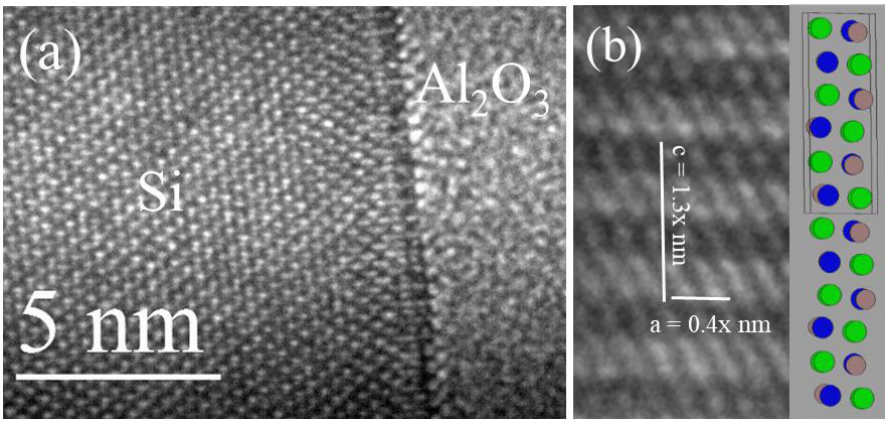


Figure 4.7. (a) A HRTEM image of Si-Al_2O_3 interface. Lattice-level information of Si in the [110] zone axis is visible. [**II**] (b) An aberration-corrected HRTEM image of a martensite-transformed AlAuCu alloy [54] with a schematic of the possible unit cell [60]. The unit cell model gives a good qualitative description of the observed image. However, the WPOA may not uphold due to the high Z number elements and the image may not be true to the actual crystal potential. The unit cell model is adapted from [60].

4.1.4 STEM, EDX and NBED

STEM and techniques related to STEM provide several possibilities for analytical TEM work. The beam is converged and condensed with apertures to provide a small probe of sub nm in diameter. The small probe is scanned on the sample so that it is always perpendicular to the sample surface. The resolution mainly depends on the size of the probe. However, signal intensity may suffer from a small probe size as the electron flux on the sample is decreased because the beam has been cut with the condensers. The transmitted electrons are collected for imaging purposes using either a high-angle annular dark-field (HAADF) detector, which collects scattered electrons, or an annular bright-field (ABF) detector which collects diffracted electrons together with the zero-order beam. Electrons scattered at different angles can be collected selectively by changing the camera length of the HAADF detector. Because the incoherent scattering angle depends heavily on the Z number, the HAADF detector may be used to collect Z contrast information ($I(HAADF) \propto Z^2$). Therefore, electrons scattered at angles of over 5° (short camera length) reveal Z contrast information in the sample.[58] As the camera length is increased (smaller scattering angle) more diffraction contrast will become visible. Figure 4.8a presents a HAADF image of a Au-Sn-Pt intermetallic system where the image was taken with intermediate camera length conditions revealing both Z and diffraction contrast information. Care needs to be taken when interpreting such mixed mode images. For example, Pt looks dark in the image despite its high Z number and the image taken in the dark-field conditions.

The STEM-EDX can be utilized in a similar fashion as SEM-EDX: the beam is scanned on the sample and emitted x-rays are collected pixel by pixel. The spatial minimum size of a pixel containing chemical information is considerably smaller compared to bulk specimens though. Figure 4.8b highlights the capabilities of STEM-EDX which enabled the analysis of a thin PtSn layer. However, despite the spatial superiority of STEM-EDX compared to SEM-EDX the quantitative accuracy is not any better or even worse as with SEM-EDX. The quantitative analysis relies on so called k factors which may not be well known and can be inaccurate for substances that are composed of greatly differing atomic numbers [64].

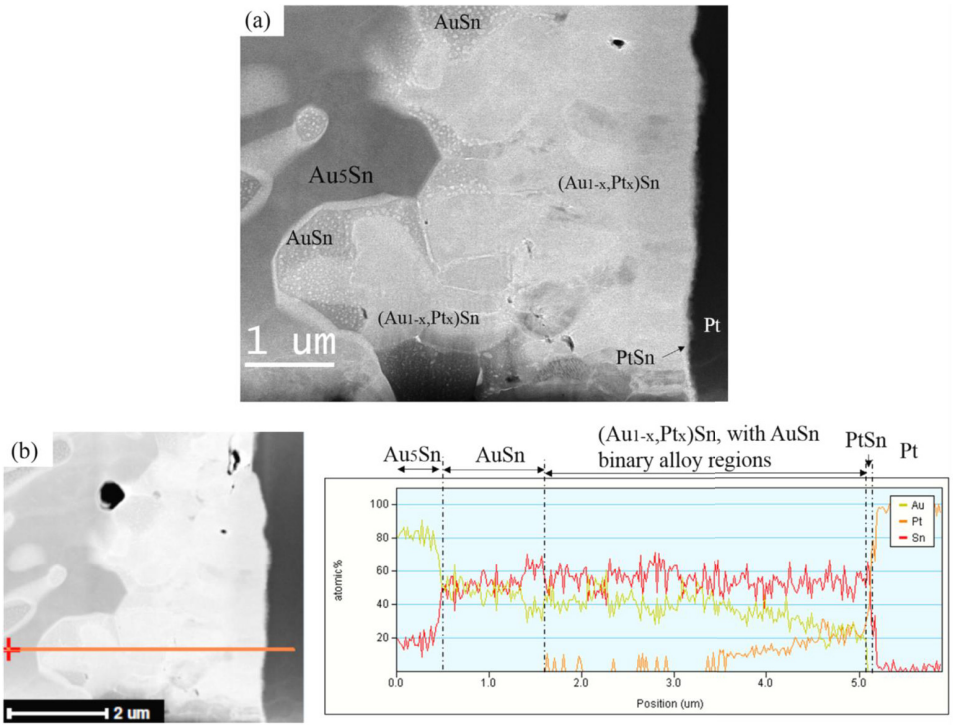


Figure 4.8. (a) A STEM-HAADF image of a Au-Sn-Pt intermetallic system showing both Z and diffraction contrast. (b) An EDX line scan was conducted to find the elemental compositions of the intermetallic phases.[65]

In addition to STEM and STEM-EDX, which were used in Publications [**II**] and [**III**], STEM was used in the strain characterization of epitaxial III-nitride thin films used in HEMTs [22,66]. Nanobeam electron diffraction (NBED) strain analysis was used in those studies and is presented here as an example of a less frequently applied analytical STEM technique. The STEM probe is made as parallel and small as possible by cutting it with very a small condenser aperture (e.g. 10-µm-diameter). This will leave the reflections at the diffraction plane almost point-like instead of disks that would be observed with a converged beam (converged beam electron diffraction, CBED). The diffraction patterns are recorded on the CCD pixel by pixel which can be then used to construct a diffraction pattern map or a line scan. The lattice spacing of each pattern is calculated and

compared to a relaxed diffraction pattern with a computer program. Figure 4.9 presents an example of the capabilities of the NBED strain mapping where the SiC substrate is considered the relaxed material to which the epitaxial AlGaN/GaN layers were compared. The gate contact metallization causes deviation in the strain of the epilayers compared to the area with no metallization.

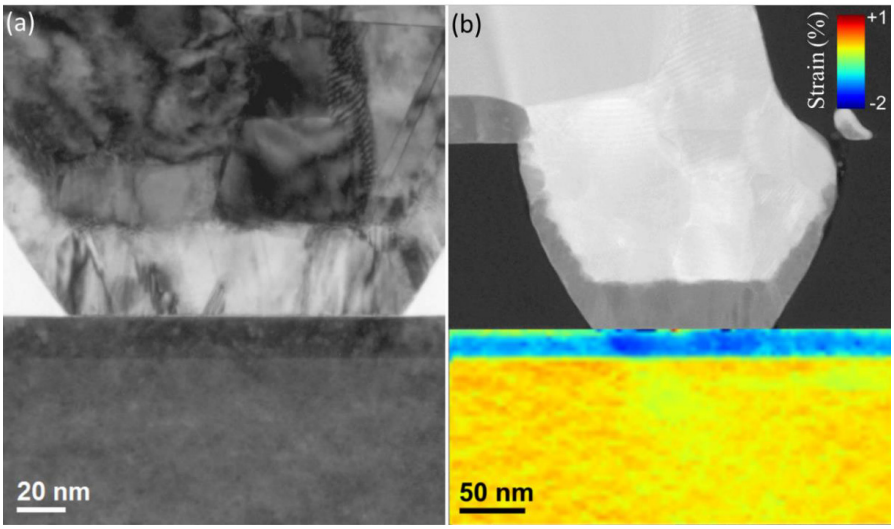


Figure 4.9. (a) A HRTEM image of a gate contact. (b) A DF STEM image overlaid with a normal strain map in the [002] direction of the hexagonal III-nitrides. [22]

4.2 X-ray Diffraction and Reflectivity

X-ray diffraction (XRD) and x-ray reflectivity (XRR) are non-destructive methods for collecting structural and chemical information.[67] Both methods are based on focusing x-rays, typically generated from a Cu target, on a sample. The x-rays interact with the sample and are diffracted in the case of XRD, or reflected in the case of XRR, to a detector. XRD is typically employed in phase analysis and can be applied to irregular sample shapes while XRR can be applied only to smooth surfaces, such as thin films, and gives information about the film thickness, surface roughness, and mass density.

XRD takes place only on a specific set of angles that fulfill the Bragg's law and the extinction rules unique to every crystal structure and combination of atoms making phase analysis possible. Therefore, diffraction is only visible at certain angles depending on the geometry of the setup and the orientation of the grains in the sample. The two common measurement geometries employed in this thesis were the symmetrical θ-2θ and the grazing incidence XRD (GIXRD). Symmetrical θ-2θ XRD detects lattice planes that lie in-plane of the substrate. GIXRD can be only applied to flat samples, such as thin films, detecting lattice planes that lie tilted in the film with respect to the substrate. Figure 4.10 presents GIXRD measurements from TMA-H_2O-based ALD Al_2O_3 films after deposition and different thermal treatments showing that the film had crystallized into the θ phase. The same alumina films were studied in [**II**], [**III**], and [**V**].

Furthermore, symmetrical θ-2θ measurements were used to approximate the biaxial stress in the AlN and Al_2O_3 films [**III**]. A biaxial stress will affect the in-plane lattice planes, i.e., a compressive biaxial stress will elongate the lattice spacing while a tensile biaxial stress causes the lattice spacing out-of-plane to be contracted. Therefore, θ-2θ, measuring lattice planes laying in-plane, can be used to approximate the level of biaxial stress if the Young's modulus, the Poisson's ratio, and the original lattice spacing are known. However, the correct, relaxed lattice spacing is typically not known and other methods, such as the $sin^2\psi$, can be applied to obtain more accurate information for calculating biaxial stresses [17].

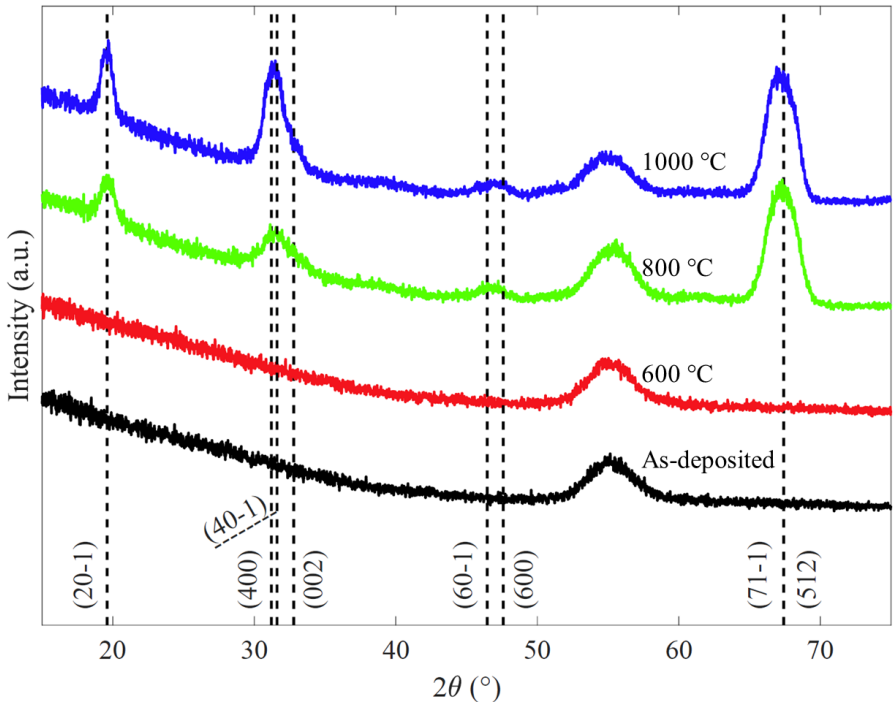


Figure 4.10. GIXRD measurements conducted on TMA-H_2O-based ALD Al_2O_3 films. The films have crystallized after the 800 and 1000 °C thermal treatments which took place in a N_2 atmosphere for one hour. Various alumina phase diffractograms were compared to the GIXRD data. θ-Al_2O_3 indexing gave the best match [68]. **[II]**

Figure 4.11 presents the principle of XRR and a measurement of an ALD AlN film. The measurement needs to be compared against a simulated fit whose variables include the film thickness, film surface roughness, and film mass density. The substrate parameters need to be included also but they are typically known. Interfacial layers, such as the substrate oxide and an oxidized film surface, can be also included in the model but should be first confirmed with other methods before being included in the XRR model.

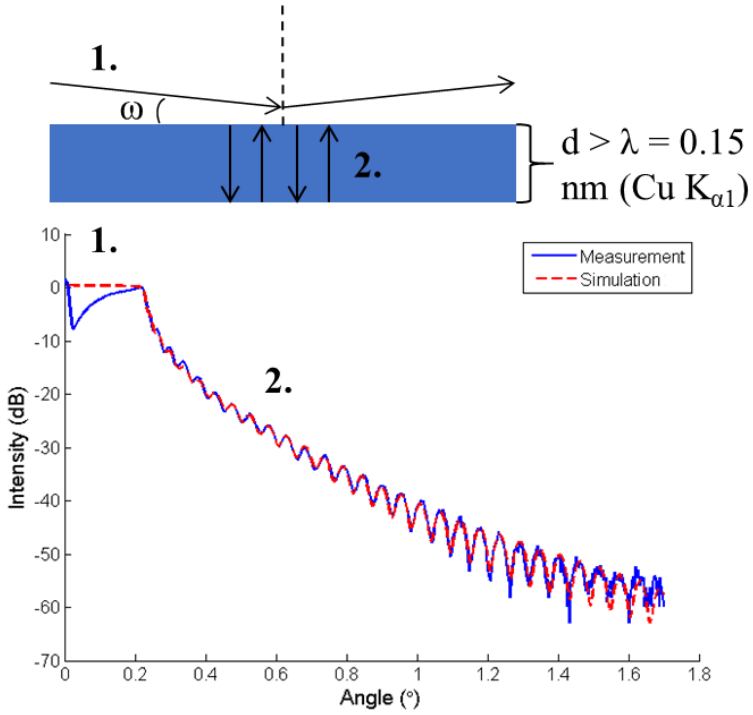


Figure 4.11. The XRR principle, measured data and a simulated fit. 1. The x-rays reflect from the film until ω grows large enough. The cut-off angle depends mainly on the film density. 2. The x-rays start to penetrate the film. Reflections at the interface between the film and substrate take place causing periodic oscillation (constructive vs destructive interference) in the film. The measured data is fit to a physical model where the variables include the film thickness, film surface roughness, and film mass density. The fit was conducted with a program developed in [69].

4.3 Time-of-flight Elastic Recoil Detection Analysis

Composition analyses were carried out in this thesis with time-of-flight elastic recoil detection analysis (ToF-ERDA) at the University of Jyväskylä.[70] The benefits of ToF-ERDA are the capability to detect light atoms encountered in AlN, Al_2O_3, and other ALD films including impurities such as hydrogen, the analysis is quantitative, and depth profiling is possible. Quantitative analysis of hydrogen is critical for the reliability of the films as the trapped hydrogen may outgas during high-temperature processing causing voiding in applications such as SOI [71] or film blistering [72]. Other common impurities in ALD films, such as carbon, can also outgas during high-temperature processing or affect the phase stabilities by hindering crystallization [26]. The reader is referred to [73] for a comparison between typical composition analysis methods for detecting impurities in thin films.

ToF-ERDA is an ion beam technique utilizing heavy elements, such as Cu and Cl, accelerated to energies in the MeV range. The ion beam is forwarded into the sample where elastic recoil takes place between the target atoms and the high-energy ions. The target atoms are recoiled out of the sample while the heavy ions scatter deeper into the sample micrometers below the region of interest where

the ions get implanted. Therefore, ToF-ERDA is also considered to be non-destructive as it does not severely damage the film being analyzed. The recoiled atoms are analyzed within the flight-tube (i.e. for the time-of-flight of the atoms) together with their energy to resolve their masses and to conduct depth profiling.[33] Figure 4.12 presents an example of ToF-ERDA data demonstrating the high purity of the ALD Al_2O_3 that was used in publications [**II**], [**III**], and [**V**].

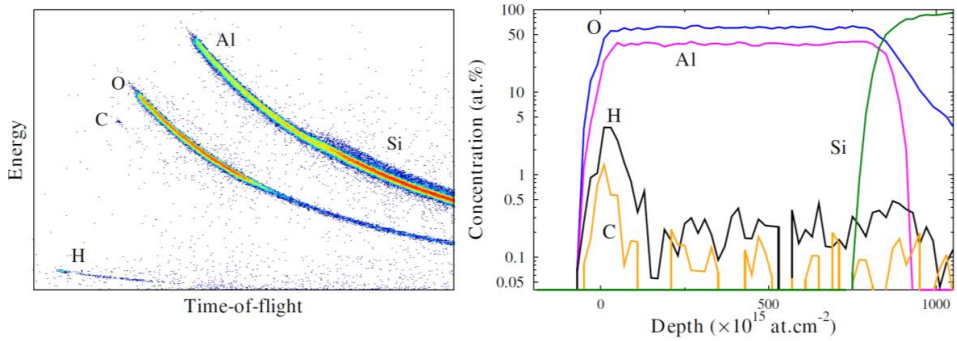


Figure 4.12. A time-of-flight – energy (ToF-E) histogram and the corresponding depth profile of an as-deposited ALD Al_2O_3 film on silicon. The ToF-E histogram is typically presented to demonstrate the high quality of the measurement data. The depth profile demonstrates the detection capability of the light impurity elements within a light element matrix. [**V**]

5. ALD Film Stability

This section presents the results achieved in Publications [**I**]–[**III**] and [**V**]. Publication [**I**] focused on ALD AlN and its thermal stability, while Publications [**II**], [**III**], and [**V**] were concerned with ALD Al_2O_3 on Si (100) surfaces and its stabilization for processability. The ALD AlN process can be considered still somewhat recent with new publications coming on a regular basis about the process development such as Publication [**IV**]. The thermal ALD Al_2O_3 on the other hand is one of the best characterized ALD processes and can be considered more mature. Therefore, the emphasis of the results with AlN was in process development (Section 3.2) while Al_2O_3 was studied more from the perspective of processability in an industrial clean room environment.

5.1 Thermal Budget

A thermal budget is the total thermal energy transferred into the device during processing. For example, processes such as dopant activation and diffusion, and CVD require elevated temperatures to take place. Dopant activation and diffusion can be realized by exposing the wafer to very high temperatures for a very short time (seconds) in rapid thermal processing while CVD can take place at a lower temperature but may require much longer times (minutes). Despite the processing temperatures are completely different, their impact on the thermal budget may be similar due to the differences in the processing times.[13,74]

Many chemical processes obey the Arrhenius law where reaction kinetics are exponentially increased with respect to the temperature. Therefore, also adverse effects, such as unwanted diffusion and reactions between two dissimilar materials, or decomposition, are exponentially accelerated once exposed to the elevated processing temperatures. A thermal budget limit must be then realized for the bill of materials used in the particular design. High-temperature processing may be endured within the first steps of the bare wafer processing but once the complexity of the design and the bill of materials increases, the temperature limit becomes lower. The thermal limitations and also the thermally-activated beneficial processes, such as metal contact annealing, of the used materials have to be understood to ensure defect-free processing.

5.2 Thermal Stability

In many cases the ALD deposition takes place before various other processing steps during which the film may experience elevated temperatures. Therefore, the thermal stability of the film plays a big role on the processability. Poor thermal stability can mean three things. First, the film may react with the atmosphere. Second, the film may react with the other materials that it is in contact with. Third, the film may outgas volatile products. However, it should be noted that if the behavior of the film is predictable and well characterized any of these reactions may be also exploited and can in fact improve the processability. For example, controlled reactions with the substrate may further enhance the adhesion between the film and the substrate.

The oxidation of AlN and other nitrides with an oxygen-containing atmosphere is governed by the Gibbs free energy change ΔG [75]:

$$\Delta G = \Delta G^0 + RT \ln\left(\frac{p_{N_2}^{\frac{2}{3}}}{p_{O_2}}\right) \tag{5.1}$$

$$= -RT \ln\left(\frac{p_{N_2}^{\frac{2}{3}}}{p_{O_2}}\right)_{equilibrium} + RT \ln\left(\frac{p_{N_2}^{\frac{2}{3}}}{p_{O_2}}\right) \tag{5.2}$$

$$= -690 + 0.064 * T + \frac{RT}{1000} \ln\left(\frac{p_{N_2}^{\frac{2}{3}}}{p_{O_2}}\right) [\text{kJ/mol}] \tag{5.3}$$

where ΔG^o is the standard Gibbs free energy change for the oxidation, R is the gas constant, T the temperature, and p's are partial pressures of nitrogen and oxygen. Based on Equation 5.3 the standard reaction for the oxidation of AlN to Al_2O_3 is favorable over a wide range of temperature and partial pressures. Nevertheless, the total driving force depends on the partial pressure ratio of nitrogen and oxygen. Figure 5.1 highlights the difference in the oxidation behavior of sputtered AlN films in atmospheres with drastically different oxygen partial pressures (air 0.21 atm vs. N_2/H_2 10^{-16}-10^{-24} atm depending on the temperature).

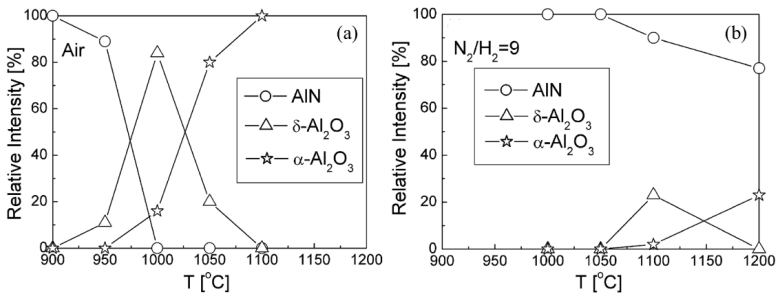


Figure 5.1. The relative XRD intensities of sputtered and crystalline AlN, δ-Al_2O_3, and α-Al_2O_3 phases after two hours of annealing the AlN at different temperatures. Oxidation behavior in air (a) and in forming gas (b). The oxidation of AlN in air takes place at lower temperatures than in forming gas. Adapted from [75].

Consequently, crystallizing AlN starting from an amorphous structure may not be feasible due to the unfavorable thermodynamics which dictate that AlN tends to oxidize. However, amorphous or nanocrystalline AlN could also provide to be useful in various applications and has proven to be a stable hard mask in SF_6-based plasma etching [76]. The thermal stability of amorphous AlN was investigated in [**I**]. It is known that the PEALD-based AlN films may contain hydrogen up to more than 20 at.% [30]. It was not clear though how the films would behave in vacuum annealing conditions and whether it would be possible to drive out the hydrogen. TMA-based PEALD AlN films were deposited at 200 °C, as described in Section 3.2, and consequently annealed between 400 and 1000 °C for one hour at the corresponding peak temperatures. The ToF-ERDA results showed a considerable amount of impurities in the films (Fig. 5.2.) The amount of hydrogen decreased due to the thermal treatments. If additional layers were to be deposited on such AlN films, further thermal treatments could cause bubbling or delamination of the layers due to the outgassing hydrogen. Furthermore, the films began to oxidize at the higher temperatures despite the high vacuum conditions. It was not completely understood whether the oxidation took place during annealing, or if additional oxidation took place after the annealing as discussed in [**I**].

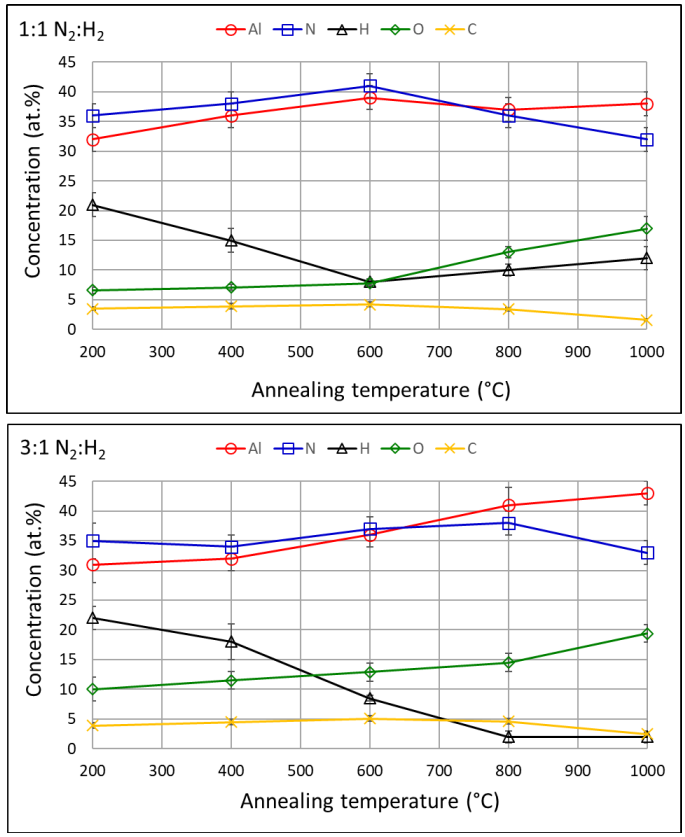


Fig. 5.2. ToF-ERDA elemental composition data of 1:1 and 3:1 N_2:H_2 flow AlN films as a function of annealing temperature. The composition data are from the midsections of the films ignoring the surfaces. [**I**]

The development of microstructure of the TMA-based films was also investigated with TEM. Figure 5.3 presents cross-sectional TEM images of the as-deposited and 1000 °C annealed films. Most notably, a small degree of crystallization had taken place from the as-deposited amorphous structures. However, as seen from Figure 5.2 ERDA data, the stoichiometry of the films had started to drift from the AlN 1:1 ratio at the higher annealing temperatures indicating the crystallizing structures may not be AlN. It was therefore concluded that when starting from similar compositions, it might not be possible to crystallize the films into the desired hexagonal pure AlN. Compared to the literature there are reports of crystalline PEALD AlN being deposited at 200 °C [38,77]. These films also have some O, C, and H impurities although less than in Fig 5.2. The amount of hydrogen was not quantitatively analyzed in either study. Recently, more reports of TMA-based AlN processes at high temperatures (above 400 °C) have emerged which display promising results of crystalline, oriented AlN [29,78]. The crystalline AlN films are expected to be more robust against oxidation and more stable during high-temperature processing. However, the amount of hydrogen remains unknown in the latest and so far best quality TMA-based ALD AlN films.

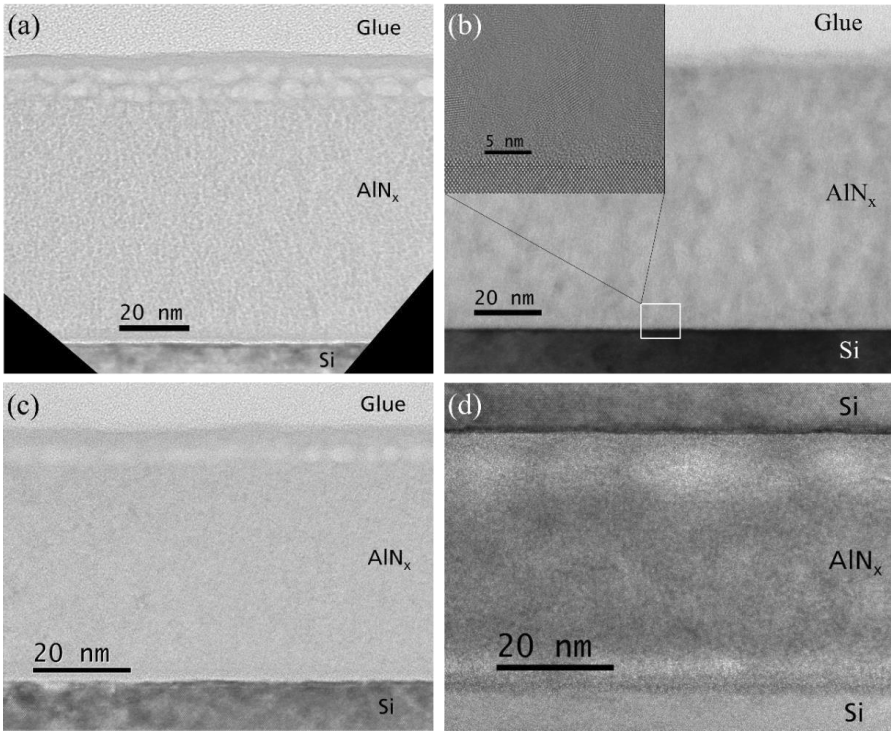


Figure 5.3. TEM images of as-deposited and annealed AlN films. (a) 1:1 N_2:H_2 as-deposited. (b) 1:1 N_2:H_2 annealed at 1000 °C in high vacuum. (c) 3:1 N_2:H_2 as-deposited. (d) 3:1 N_2:H_2 sample annealed at 1000 °C in high vacuum (the sample is from a different deposition run and was used in a bonding experiment). Annealed films show a small degree of crystallinity that could not be assigned to the hexagonal AlN based on the FFTs. **[I]**

ALD Al_2O_3, on the other hand, is expected to be thermodynamically stable during high-temperature treatments. It is therefore possible to crystallize amorphous ALD Al_2O_3 with heat treatments as discussed in [**II**] and [**V**]. However, just like ALD AlN, also ALD alumina may have impurities such as hydrogen and carbon which can adversely affect its stability during processing. Indeed, hydrogen-induced blistering of ALD alumina is an issue widely recognized in Si-based solar cell manufacturing where ALD alumina provides excellent surface passivation [79–82]. Blistering takes place during the firing step in the solar cell processing whose purpose is to improve the interfacial quality between Si and Al_2O_3. The root-cause for the blistering is not well understood. Hydrogen is released from the alumina films during annealing which gets trapped at the interface between Si and alumina. It has been proposed that the hydrogen gas pressure causes the blister formation. However, Xie et al. [83] recently showed that that in order to initiate the blister formation from a nm-order defect site, an unrealistically high gas pressure of tens of gigapascals would be required. Therefore, a subcritical gas bubble should grow first before the macroscopic delamination and blister formation can occur. The study of Xie et al. was conducted on a bulk Al-Al_2O_3 system though, whereas in [**III**] the blistering mechanism was studied in ALD Al_2O_3 on Si in HV-annealed samples. Figure 5.4 shows that similar to the study of Xie et al. cavitation of the substrate had taken place at a blister site.

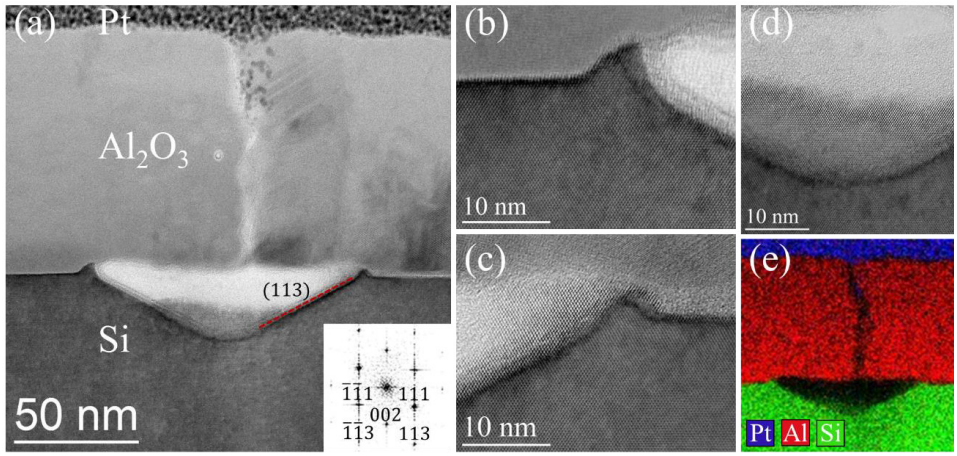


Figure 5.4. HRTEM images of the Al_2O_3 film annealed in HV at 1000 °C. (a) An overview image of the blister site shows a cavity in Si with a crack extending from the cavity through the film. The inset shows the FFT image of Si. (b)-(d) Higher magnification images of the cavity area did not show defects in Si. The accumulated Si at the edges was stacked epitaxially. (e) An EDX map did not indicate interdiffusion between alumina and Si. [**III**]

On the contrary, nitrogen, hydrogen, and low vacuum annealing at similar temperatures did not produce blisters. [**II**], [**V**] The annealing processing window to produce crystalline, mechanically, and chemically stable Al_2O_3 was proposed in [**V**]. Figure 5.5 summarizes the different surface states of the alumina films that resulted from the different annealing environments. Above 1050 °C

annealing caused cracks in the films. 1300 °C annealing in H_2 changed the appearance of the film completely. Annealing at 1000 °C in high vacuum conditions caused blistering. ALD Al_2O_3 films that were crystalline and free of macroscopic defects were achieved by annealing the films up to 1050 °C in H_2 and N_2 atmospheres. The films were deposited on Si (100). The type of ALD Al_2O_3 films in Figure 5.5d are expected to be stable during high-temperature processing in temperatures below the annealing temperature and resistant to aggressive chemicals as described in the next chapter.

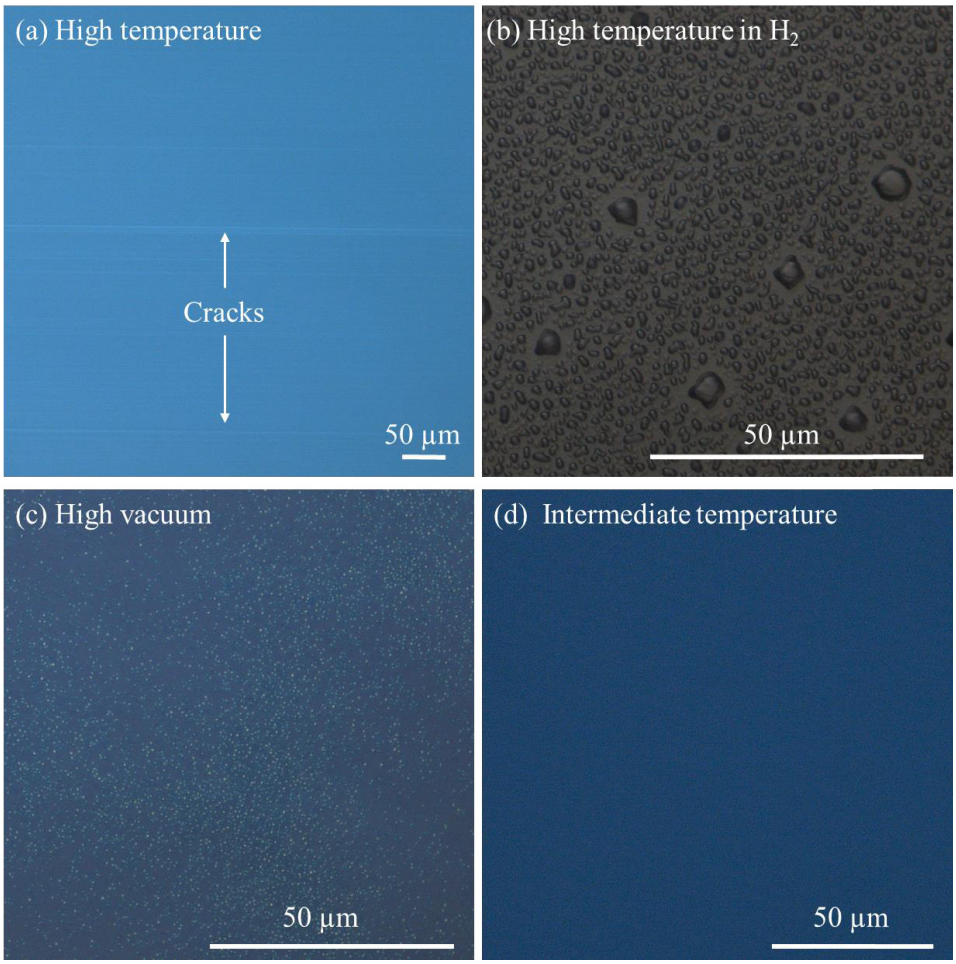


Figure 5.5. (a) Cracks were seen in films that were processed at temperatures above 1050 °C. (b) The alumina films annealed in 1-bar H_2 at 1300 °C completely changed their visual appearance and did not show XRD peaks. A similar observation of the deterioration of ALD alumina at very high temperatures has been made by Zhang et al. [52]. (c) High vacuum annealing at 1000 °C caused blistering. (d) Annealing in a suitable environment up to 1050 °C produced defect-free crystalline Al_2O_3 films. **[V]**

5.3 Chemical Stability

Chemical stability is understood in this thesis as the film's ability to resist changes in its composition in environments that do not include high temperature thermal treatments. Examples of chemical stability can be a stable composition in room-temperature storage or resistance to dissolution or corrosion in wet environments. Chemical stability of ALD films is of paramount importance as structural, protective, and functional coatings are expected to maintain their performance over the lifetime of the device or during processing. Especially ALD Al_2O_3, TiO_2, and their nanolaminates have attained considerable interest as barrier coatings [84–88]. Furthermore, ALD Al_2O_3 can be an excellent hard mask in HAR micromachining with improved performance compared to SiO_2 [10,11]. However, ALD alumina in the as-deposited state is amorphous and susceptible to water corrosion [84,87,88], while good stability has been demonstrated with Al_2O_3/TiO_2 nanolaminates [88] and crystalline ALD Al_2O_3 [84,89,90].

The chemical stability of one-layer ALD Al_2O_3 films was studied in [**II**]. The simple one-layer alumina was selected due to the maturity of the deposition process making it a feasible candidate for industrial-scale processing. However, in order to implement the ALD Al_2O_3 processing in an industrial cleanroom environment the film has to remain stable in wafer cleaning solutions used in the Radio Corporation of America cleaning procedure [91,92]. The ALD Al_2O_3 films were annealed in HV conditions and in a nitrogen atmosphere at 1000 °C and were subsequently etched in SC-1 (ammonium hydroxide and hydrogen peroxide) and de-ionized water (DIW). The HV-annealed films showed blistering studied in [**III**] and were not selected for the chemical stability investigations. The stability of the as-deposited films was poor as demonstrated in [**II**], while the crystallized films (annealed in nitrogen) showed stability in SC-1, DIW, and dilute HF. Figure 5.6 demonstrates the behavior of the films after SC-1 and HF treatments.

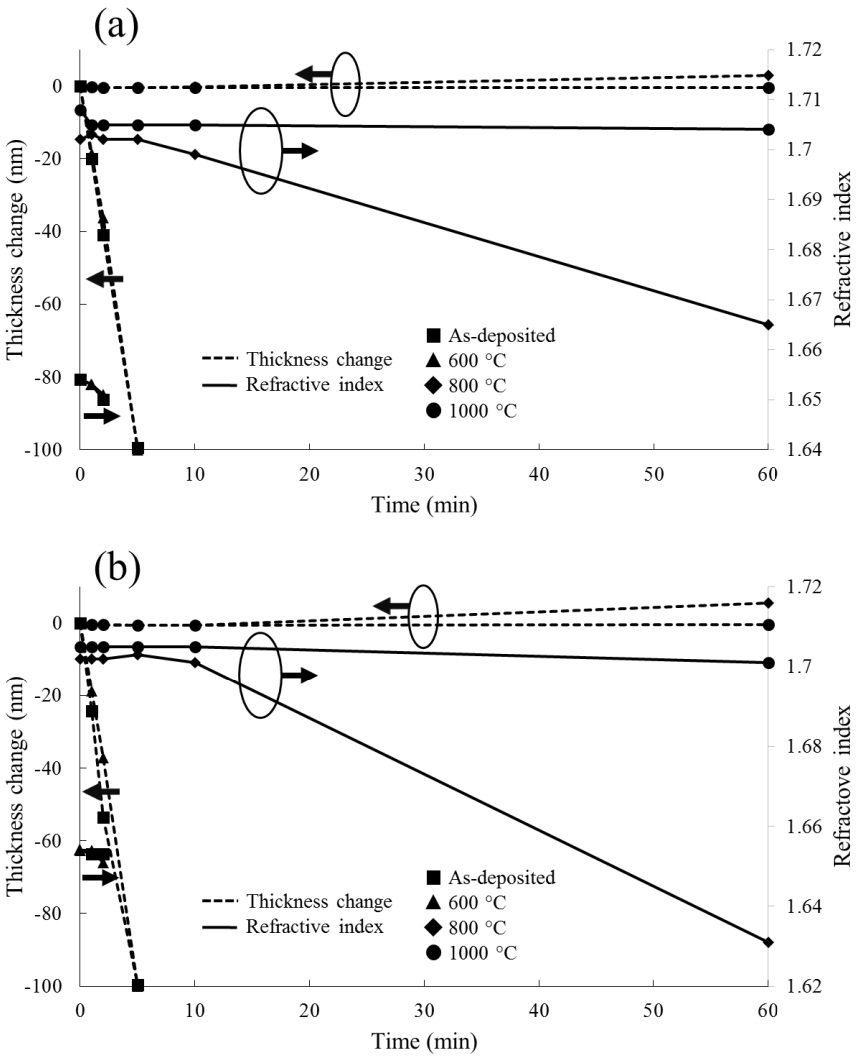


Figure 5.6. The changes in thicknesses and refractive indices of TMA-H_2O-based ALD Al_2O_3 films with respect to immersion time. (a) SC-1, and (b) HF. The dashed lines represent the thickness changes and solid lines the changes in the refractive indices. [**II**]

Despite the films annealed at 800 °C showed stability over the first minutes of immersion, a prolonged exposure had caused changes in their refractive indices and thicknesses. Both 1000 °C and 800 °C N_2-annealed films had crystallized to the same θ phase. However, TEM inspection revealed that the 800 °C annealed film in SC-1 had deteriorated at the Si-film interface and along its grain boundaries. It was concluded that to obtain fully chemically stable ALD Al_2O_3 it would be desirable to obtain crystallization-wise developed θ phase alumina. Figures 5.7 and 3.6 present TEM images of the deteriorated film and fully stable film, respectively.

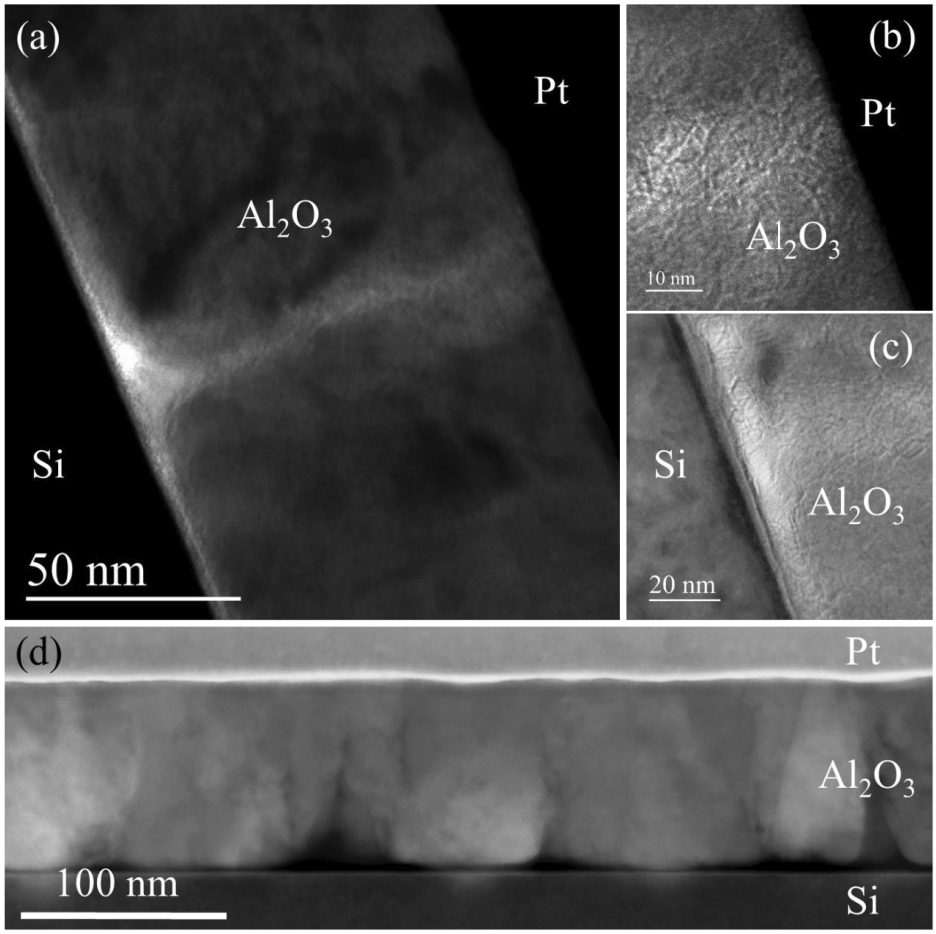


Figure 5.7. TEM images of the sample annealed in N_2 at 800 °C and immersed in SC-1 for 60 minutes. (a) A BF-TEM image at a defect site showing that most of the chemical attack had taken place at the substrate interface. HRTEM images of the defect site at the surface (b) and the substrate interface (c). (d) The dark areas indicate corrosion in the DF STEM image. **[II]**

5.4 Crystallization

Crystallization of an amorphous solid (or liquid) starts from nucleation centers. The driving force ΔG_r for a crystalline, spherical particle of radius r to form is [93,94]:

$$\Delta G_r = 4\pi r^2\gamma + \frac{4}{3}\pi r^3 \Delta G_v \tag{5.4}$$

where γ is the surface energy between the particle and the amorphous matrix and ΔG_v is the Gibbs free energy per unit volume of the crystalline particle. The first term is positive and represent the energy required to form a new surface, whereas the second term is negative owing to the decrease in enthalpy of the ordered particle. Since the terms depend on the second and third powers of the radius of the nucleation center, it is evident that there is a particle of a critical

radius r^* that induces growth of that center into a crystallite. The critical energy to overcome for such a nucleus is:

$$\Delta G^* = \frac{16}{3}\frac{\pi\gamma^3}{\Delta G_v^2} \tag{5.5}$$

Equation 5.5 describes the energy barrier for homogenous nucleation where nucleation takes place within the amorphous solid. Contrary to the homogenous nucleation, heterogeneous nucleation includes wetting of a catalyst surface such as impurities, the substrate, or the surface of the film. The critical energy ΔG^* is modified by considering the surface energies of the catalyst (e.g. substrate), crystallite nucleus, and amorphous matrix:

$$\Delta G^* = \frac{16}{3}\frac{\pi\gamma_{nucleus-amorphous}^3}{\Delta G_v^2}\frac{(2+cos\theta)(1-cos\theta)^2}{4} \tag{5.6}$$

Therefore, the critical energy depends on the wetting that takes place on the catalyst as illustrated in Figure 5.9. The surface energy between the catalyst and the amorphous material plays a role in the crystallization when heterogeneous nucleation takes place.

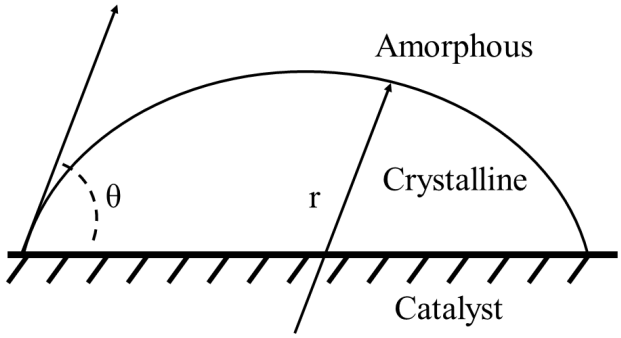


Figure 5.9. The wetting of the catalyst surface modifies the critical nucleation energy that needs to be overcome for crystallization to take place.

In practice, most bulk materials exhibit heterogeneous nucleation.[95] However, the crystallization of amorphous thin films (or ALD films) is relatively little studied and it is also possible that homogenous nucleation could be experienced. For example, NiTi thin films have been studied due to its shape-memory alloy effect for MEMS applications [96–98]. The films were sputtered in the amorphous form and crystallized in a controlled manner to tailor the microstructure which heavily affects the shape-memory properties. In the NiTi films it was found that the films in fact crystallized via the homogenous nucleation from the bulk of the films [96]. The root-cause was likely that the films became oxidized at the surface, and at the substrate side interdiffusion had taken place. As both reactions modified the Gibbs free energy per unit volume of the amorphous NiTi, the homogenous nucleation in the bulk became favored.

The crystallites grow while more crystals keep nucleating. At some point the complete film has crystallized. The crystal size distribution is therefore determined based on these two competing processes: nucleation and growth. Controlling both with temperature also provides the possibility to control the microstructure of the film. Crystal growth continues if the annealing process is prolonged at an elevated temperature because of the energetically unfavorable large surface area of small grains.

Typically, crystallization kinetics – the studies of nucleation and growth rates – are studied utilizing differential scanning calorimetry (DSC). Both isothermal and ramped experiments provide information about the changes of the latent heat in the system. The DSC experiments provide the required data to find critical parameters related to crystallization kinetics which then can be used to deduct information such as the type of crystal growth: 1, 2, or 3-dimensional, diffusion-controlled growth, or polymorphous crystallization (no long-range mass transportation required). However, DSC experiments have practical limitations with respect to ALD films. Typically, several milligrams of material are required, preferably without the substrate, to improve the signal-to-noise ratio. Consequently, the number of DSC experiments are limited on ALD films [99].

Defining the final (micro)structure of the crystallized thin film is obviously important besides understanding the crystallization kinetics. The structure investigations typically involve XRD analysis such as in [**II**]–[**V**]. Furthermore, TEM techniques provide detailed information about the interfacial structure, film morphology, and surface structure investigated in [**II**]–[**IV**]. Several polymorphs can exist for a given material. Elevated temperature drives the transformations. The increased temperature will cause the atoms of a crystal to accumulate higher vibrational energy. As temperature increases crystalline solids tend to phase change into crystal structures that can accommodate the vibrational energy better [39]. For example, systems with a higher symmetry can accommodate more degrees of freedom for vibrational states. The transformations depend on many aspects such as the original structure and chemical composition of the material.

Levin and Brandon [100] propose the temperature dependent transformation route for amorphous Al_2O_3 as follows: amorphous → γ → δ → θ → α-Al_2O_3 where several phases can co-exist. However, other transformation routes exist too and, for example, in [**III**] and [**V**] ALD Al_2O_3 that was annealed at 1000 °C in high vacuum conditions showed κ [101], θ [68], and α [102] phases, whereas in [**II**] the same film annealed in nitrogen at 1000 °C showed only the θ phase [68]. In [**V**] the crystallization kinetics of ALD Al_2O_3 were studied in situ via reflectance measurements during the annealing while XRD was utilized ex situ to analyze the resulting phases. Figure 5.10 presents four different annealing runs conducted in different atmospheres at a ramp rate of 0.2 °C/s. A dip in the reflectance is visible around 850 °C associated with a clear change in the structure of the films. Additional annealing runs were conducted by holding the temperature just before the dip in the reflectance, stopping the annealing at 950 °C, and stopping the annealing in 1-bar H_2 close to the point where a drastic dip in the re-

flectance is seen at 1300 °C in Figure 5.10 (Transition 4). Furthermore, additional films were annealed in HV conditions at 1000 °C with a dwell time of one hour. The resulting crystalline structures were then investigated ex situ with XRD (Fig. 5.11). It was deducted that the vacuum annealing, which induced a different set of crystallized phases, modified the surface energy of alumina. The modified surface energy caused either heterogeneous nucleation to the mixture of three phases or phase transformations after the initial crystallization. Nanocrystalline Al_2O_3 is known to show different phase stability compared to bulk Al_2O_3 where the α phase is the most stable one [103,104]. Therefore, the films that crystallized purely into the θ phase in Figure 5.11 did not undergo phase transitions at the higher temperatures. Finally, crystallization can be controlled by depositing the film on a template surface that modifies the surface energy at the substrate-film interface [21]. For example, Zhang et al. [52] deposited ALD Al_2O_3 on Si (111) substrates which crystallized into the α phase after annealing.

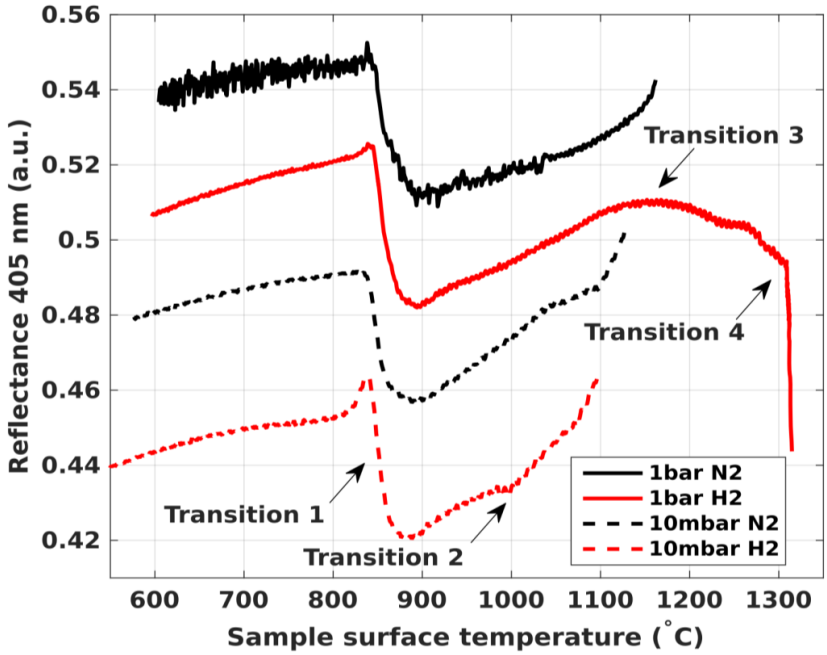


Figure 5.10. The surface reflectances of alumina films annealed in different atmospheres at the ramp rate of 0.2 °C/s. The dip around 850 °C was associated with the crystallization of the films. The root cause of Transitions 2 and 3 remained unclear. [**V**]

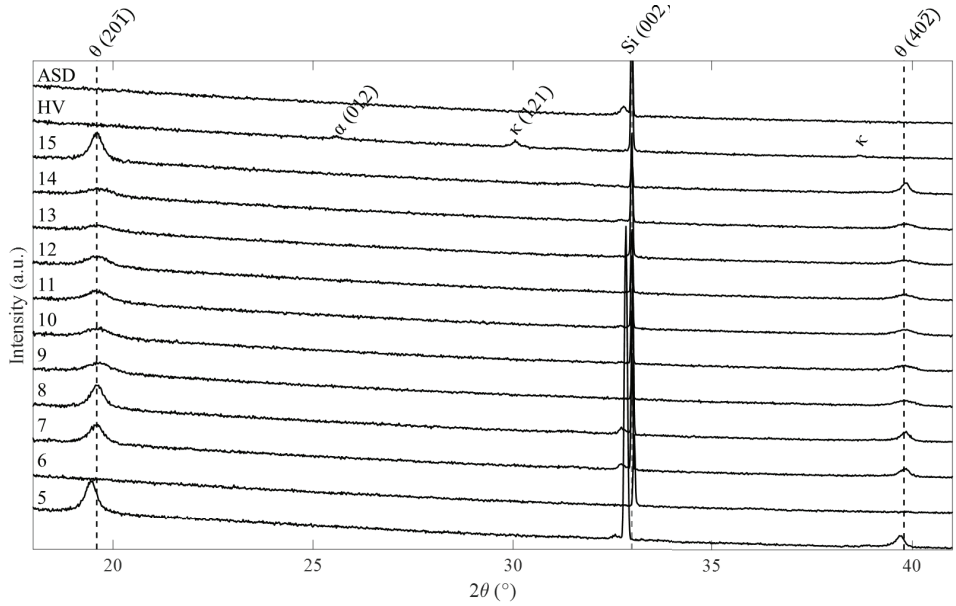


Figure 5.11. Diffractograms of many ALD Al_2O_3 annealing runs conducted in different atmospheres. The as-deposited (ASD) film shows no peaks (amorphous) and the high vacuum (HV) -annealed film shows a mixture of phases compared to the other crystallized alumina films which were best indexed with only the θ phase indexing. The numbers 5–15 refer to the experiments detailed in [**V**].

6. Prospects

In discussions with the ALD researchers it is often brought up that TMA begins to decompose at around 370 °C [28,43]. Therefore, the TMA-based processes above that temperature may not be in the strictest sense ALD type growth. However, such temperatures are still reasonably low compared to, for example, metal-organic chemical vapor deposition (MOCVD) where above 1000 °C is usually utilized in AlN deposition. TMA-based plasma processes above 370 °C could offer new perspectives for depositing high-quality ALD AlN as demonstrated in References [29,78]. The amount of hydrogen should be still characterized in the high-temperature ALD AlN films. Depending on the application hydrogen may cause issues. For example, using ALD AlN in HEMT stress engineering as a buffer layer means that the film would be exposed to temperatures above 1000 °C if MOCVD is used for the subsequent III-nitride layers. Obviously in the best case ALD could be used for the complete deposition process of all the required nitrides. Promising results have been demonstrated in [38] although the crystalline quality was not enough for piezoelectric materials. Using the PEALD process also offers stress tuning for said buffer layers as demonstrated in [**IV**]. Amorphous AlN could be also utilized in applications were low surface roughness is required. Amorphous, rather pure, and low hydrogen ALD AlN could be achieved by conducting vacuum annealing at around 700 °C. However, the annealing behavior depends on the original stoichiometry and impurities. It could be also possible to improve the crystallinity of ALD AlN by annealing in forming gas below 1000 °C, which would likely decrease the amount of hydrogen too, but its effect on the stress state of the film is unknown.

The decomposition of TMA has, in fact, shown not be an issue in the ALD Al_2O_3 process [**II**]. No adverse CVD-type effects were seen – the GPC was reasonable (thickness control), non-uniformity minimal, stoichiometry close to the ideal, and the films had a minimal amount of impurities. The second precursor, for example H_2O, is very reactive with the TMA-saturated surface though which can help in minimizing impurities that could come from the decomposition of TMA. Deposition above 450 °C, the temperature that was used in [**II**] and [**V**], might in fact produce crystalline alumina films although the decomposition might also become dominating in some point too. Possible problems with TMA self-decomposing can be circumvented by using $AlCl_3$ for alumina deposition. Crystalline ALD Al_2O_3 from $AlCl_3$ has been demonstrated by Aarik et al. [40] but the >600 °C deposition temperature for crystalline alumina can be rarely achieved with ALD reactors. Nevertheless, using the 450 °C process from Beneq

Oy and the alumina films being annealed in nitrogen at 1000 °C producing crystalline, chemically stable films could be utilized in applications where uniformity, thickness control, and thermal and chemical stability are needed. One such application is SOI. Figures 6.1 and 6.2 present TEM images of a successfully fabricated SOI substrate on 150 mm wafers. The process was based on depositing also an additional SiO_2 layer which was used as the surface for direct bonding. The ALD Al_2O_3 was crystallized at 1000 °C in nitrogen, its surface was chemically cleaned, the SiO_2 was deposited on it and further annealed to remove hydrogen, the SiO_2 polished and finally direct bonded to a handle wafer.

Figures 6.1 a and b show the polycrystalline θ-Al_2O_3 expected based on [**II**]. What is surprising is that the Si-Al_2O_3 interface does not have a similar interfacial layer or at least it is not quite as thick (Fig. 6.1c vs. 3.6c). It should be noted that the SOI stack has experienced, in addition to the Al_2O_3 crystallization, two additional heat treatments (SiO_2 annealing and bonding annealing). The interfacial reactions are proposed to follow a sequence: Al_2O_3 and Si do not mix initially → at higher temperatures interdiffusion takes place, the interfacial layer is initially amorphous → the interfacial layer crystallizes. Another option could be different defocus conditions but the interfacial layer in the bare annealed film is also visible in BF TEM and DF STEM images (Figures 3.6 a and e). Continuing with the Al_2O_3-SiO_2 interface in Figure 6.1d, the interface is diffuse and no clear boundary is visible. The SiO_2 had been deposited on the crystallized alumina so a small amount of interdiffusion is beneficial for strong chemical bonding. Finally, the bonded SiO_2-Si interface is abrupt in a similar fashion as in a direct-bonded Si-SiO_2 pair after annealing would be expected [105]. Finally, the EDX data in Figure 6.2 show sharp interfaces and distinct layers. The characterization of the Al_2O_3-Si SOI wafers continues. For example, additional characterization is needed to understand the device layer crystalline quality, stress of the different layers, and interface adhesion strength.

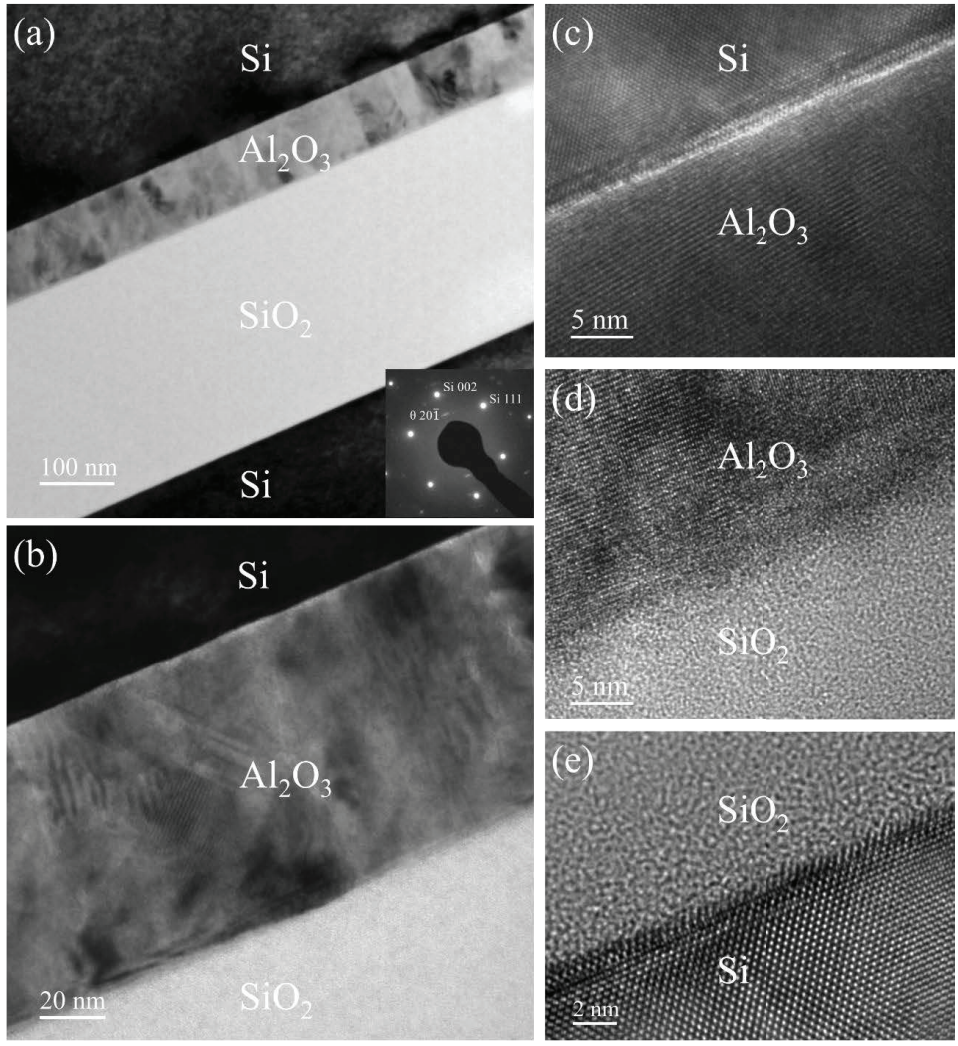


Figure 6.1. Cross-sectional TEM images of an Al_2O_3-SiO_2 SOI wafer. (a)-(b) Overview BF images showing the SOI stack, polycrystalline alumina, and the SAED pattern in the inset of (a). (c)-(e) HRTEM images of the interfaces in the same order from top to bottom as the stack in the overview images. Images courtesy of Glenn Ross.

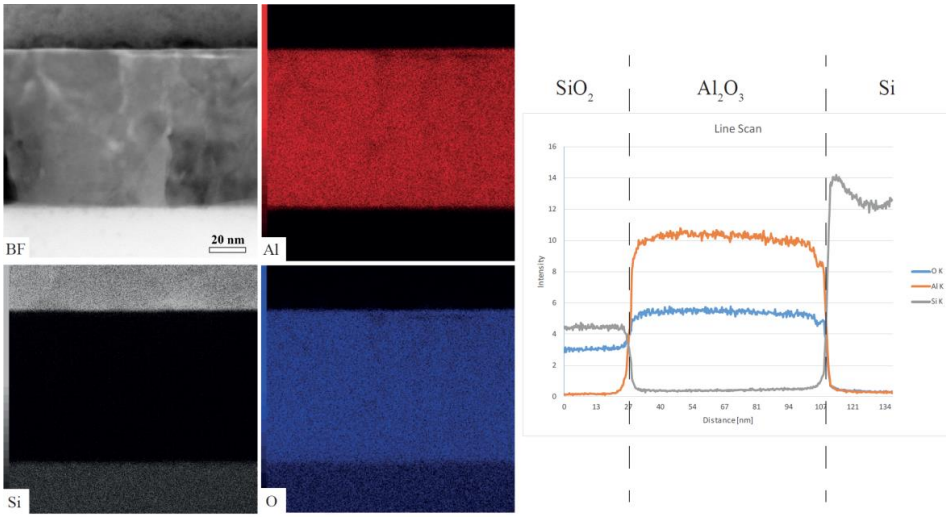


Figure 6.2. A BF STEM image and EDX mapping of the device Si-Al_2O_3-SiO_2 area of the SOI wafer. The EDX data has been collapsed into a line profile on the right which shows abrupt interfaces. The intensity of the line profile is in counts. Images courtesy of Glenn Ross.

7. Conclusions

Continued electronic device miniaturization, increasing performance, and functionality diversification driven by increasing demand impose challenges for the semiconductor industry. New solutions demand new materials and the adaptation of already-developed materials to enable them. Consequently, processing the materials requires the adaptation of new deposition tools and further process development. ALD is a versatile deposition method already established in the semiconductor industry for selected processes such as in the deposition of Hf-based gate oxides. However, despite ALD meeting many aspects demanded from a deposition method for the fabrication of semiconductor devices there are some drawbacks that inhibit the use of specific ALD materials. Most notably, many ALD materials may not be suitable for processing at the initial steps of fabrication where harsh chemicals are applied for cleaning purposes and elevated temperatures are used for various processes such as dopant activation.

TMA-based AlN deposited at 200 °C was deemed unstable at high-temperatures due to outgassing a high amount of hydrogen. Furthermore, the AlN films began to oxidize at and above 800 °C – earlier than compared to crystalline, sputtered AlN. Contrary to the TMA-based films deposited at 200 °C, AlN films deposited from $AlCl_3$ showed promising results in terms of crystallinity, stoichiometry, and the amount of impurities. Furthermore, the plasma process enabled stress tuning achieving near-zero biaxial stress. The literature also shows promising results with high-temperature (>400 °C) TMA-based ALD AlN films in terms of crystallinity and a low amount of impurities [29,78]. Many promising ALD AlN publications still share the same drawback; the amount of hydrogen is not measured due to limited access to suitable techniques such as ToF-ERDA. It should be noted though that the amount of outgassing species and the stress state may or may not be issues depending on the application and at which point of device manufacturing the film is deposited. Working closely with the design teams and understanding the requirements of the industry, keeping in mind the final application, is a must. The film material properties need to be understood along the complete process flow for successful engineering. Publications [**I**] and [**IV**] aimed at understanding the thermal stability of ALD AlN, fundamental film properties that affect the thermal stability such as stoichiometry and crystallinity, and the relationships between the processing parameters and film quality. The ALD AlN studies were more focused in process development as ALD AlN is less studied, and hence less mature compared to ALD Al_2O_3. The highlighted contributions of the AlN results are:

i) The amount of hydrogen is high in TMA-based AlN films at temperatures typically employed in TMA-based ALD processes. Hydrogen can be driven out with additional thermal treatments.
ii) Based on the literature review and $AlCl_3$-based deposition results in [**IV**], higher deposition temperatures, in the order of 500 °C, could be beneficial in depositing high-quality AlN.
iii) The stress state of the AlN films can be tuned over a wide range utilizing the plasma-enhanced process.

ALD Al_2O_3 was an example of a material that has been studied for a rather long time. Furthermore, there was a clear indication from the industry for a need of better etch stop capabilities in MEMS manufacturing for which purposes ALD Al_2O_3 has shown promise [10,11]. HAR micromachining, realized on SOI substrates, requires rather thick SiO_2 for not punching through the oxide, while ALD alumina could provide the same etch stop capabilities with a fraction of thickness. A thinner BOX could enable applications such as foldable chips as the device layer and the BOX thickness together would become flexible as the bending stiffness would decrease dramatically (second moment of area $\propto$ thickness^3) by removing the handle wafer or etching the handle wafer locally. Fabricating such SOI substrates requires the film to be chemically and thermally stable. As-deposited, amorphous ALD Al_2O_3 is not resistant to the wet chemistries used in wafer cleaning, while crystallized ALD alumina was shown to be stable and not contaminate the cleaning solutions [**II**]. A SOI prototype was finally demonstrated (Fig. 6.1) whose characterization and the associated process development continues. For example, the final stress states of the individual material layers, important for MEMS, are under investigation. Also, making the assistive SiO_2 of the demonstrated SOI thinner or completely removing it would decrease the bending stiffness. Many other applications outside the microelectronics industry, such as dental instruments, could benefit from the barrier properties of chemically and thermally stable ALD Al_2O_3 [106]. ALD Al_2O_3 was studied from the perspective of further processability due to the film deposition processes being more mature and resulting in high-quality as-deposited films. Publications [**II**], [**III**], and [**V**] studied the effects of microstructure refinement on the thermal and chemical stability of the Al_2O_3 films. The specific contributions are:

i) As-deposited, amorphous ALD Al_2O_3 films are susceptible to corrosion and dissolution in various wet chemistries employed in microelectronics manufacturing, whereas crystalline ALD alumina becomes highly resistant to chemical attack.
ii) The annealing atmosphere plays a role in the crystallization kinetics and can results in a different phase of the crystallized film as well as in defects such as blisters. Selecting the annealing conditions appropriately results in polycrystalline structure without macroscopic defects such as blisters and cracks.

References

(1) Schaller, R. R. Moore's Law: Past, Present and Future. *IEEE Spectr.* **1997**, *34* (6), 52–59.

(2) Arden, W.; Brillouët, M.; Cogez, P.; Graef, M.; Huizing, B.; Mahnkopf, R. More-than-Moore White Paper. *Version* 2010, *2*, 14.

(3) Puurunen, R. L. A Short History of Atomic Layer Deposition: Tuomo Suntola's Atomic Layer Epitaxy. *Chem. Vap. Depos.* **2014**, *20* (10-11–12), 332–344.

(4) Kelly, A. J.; Tzng, P.-R.; Chien, P.-S.; Tseng, W.-H. Method of Making a FinFET Device. Google Patents 2014.

(5) Scharf, T. W.; Prasad, S. V; Dugger, M. T.; Kotula, P. G.; Goeke, R. S.; Grubbs, R. K. Growth, Structure, and Tribological Behavior of Atomic Layer-Deposited Tungsten Disulphide Solid Lubricant Coatings with Applications to MEMS. *Acta Mater.* **2006**, *54* (18), 4731–4743.

(6) Li, J.; Broas, M.; Makkonen, J.; Mattila, T. T.; Hokka, J.; Paulasto-Kröckel, M. Shock Impact Reliability and Failure Analysis of a Three-Axis MEMS Gyroscope. *J. Microelectromechanical Syst.* **2014**, *23* (2), 347–355.

(7) Motoyoshi, M. Through-Silicon via (TSV). *Proc. IEEE* 2009, *97* (1), 43–48.

(8) Broas, M.; Demir, K.; Sato, Y.; Sundaram, V.; Tummala, R. A Comparative Reliability Study of Copper-Plated Glass Vias, Drilled with CO2 and ArF Excimer Lasers. *Electronics System-Integration Technology Conference (ESTC),* 2014; pp. 1–5.

(9) Scholten, A. J.; Smit, G. D. J.; Pijper, R. M. T.; Tiemeijer, L. F.; Tuinhout, H. P.; van der Steen, J.-L.; Mercha, A.; Braccioli, M.; Klaassen, D. B. M. Experimental Assessment of Self-Heating in SOI FinFETs. In *Electron Devices Meeting (IEDM), IEEE International*, 2009; pp. 1–4.

(10) Sainiemi, L.; Franssila, S. Mask Material Effects in Cryogenic Deep Reactive Ion Etching. *J. Vac. Sci. Technol. B Microelectron. Nanom. Struct.* **2007**, *25* (3), 801–807.

(11) Dekker, J.; Kolari, K.; Puurunen, R. L. Inductively Coupled Plasma Etching of Amorphous Al2O3 and TiO2 Mask Layers Grown by Atomic Layer Deposition. *J. Vac. Sci. Technol. B Microelectron. Nanom. Struct.* **2006**, *24* (5), 2350.

(12) Madou, M. J. *Manufacturing Techniques for Microfabrication and Nanotechnology*; CRC press, 2011; Vol. 2.

(13) Franssila, S. *Introduction to Microfabrication*; John Wiley & Sons, 2010.

(14) Miikkulainen, V.; Väyrynen, K.; Kilpi, V.; Han, Z.; Vehkamäki, M.; Mizohata, K.; Räisänen, J.; Ritala, M.; others. Photo-Assisted ALD. *ECS Trans.* 2017.

(15) Crowell, J. E. Chemical Methods of Thin Film Deposition: Chemical Vapor Deposition, Atomic Layer Deposition, and Related Technologies. *J. Vac. Sci. Technol. A Vacuum, Surfaces, Film.* **2003**, *21* (5), S88–S95.

(16) Leskelä, M.; Ritala, M. Atomic Layer Deposition (ALD): From Precursors to Thin Film Structures. *Thin Solid Films* **2002**, *409* (1), 138–146.

(17) Abadias, G.; Chason, E.; Keckes, J.; Sebastiani, M.; Thompson, G. B.; Barthel, E.; Doll, G. L.; Murray, C. E.; Stoessel, C. H.; Martinu, L. Review Article: Stress in Thin Films and Coatings: Current Status, Challenges, and Prospects. *J. Vac. Sci. Technol. A Vacuum, Surfaces, Film.* **2018**, *36* (2), 20801.

(18) Ylivaara, O. M. E.; Liu, X.; Kilpi, L.; Lyytinen, J.; Schneider, D.; Laitinen, M.; Julin, J.; Ali, S.; Sintonen, S.; Berdova, M.; Haimi, E.; Sajavaara, T.; Ronkainen, H.; Lipsanen, H.; Koskinen, J.; Hannula, S. P.; Puurunen, R. L. Aluminum Oxide from Trimethylaluminum and Water by Atomic Layer Deposition: The Temperature Dependence of Residual Stress, Elastic Modulus, Hardness and Adhesion. *Thin Solid Films* **2014**, *552*, 124–135.
(19) Koch, R. The Intrinsic Stress of Polycrystalline and Epitaxial Thin Metal Films. *J. Phys. Condens. Matter* **1994**, *6* (45), 9519.
(20) Freund, L. Ben; Suresh, S. *Thin Film Materials: Stress, Defect Formation and Surface Evolution*; Cambridge University Press, 2004.
(21) Andersson, J. M. Controlling the Formation and Stability of Alumina Phases; Doctoral dissertation, Institutionen för fysik, kemi och biologi, 2005.
(22) Broas, M.; Graff, A.; Simon-najasek, M.; Poppitz, D.; Altmann, F.; Jung, H.; Blanck, H. Microelectronics Reliability Correlation of Gate Leakage and Local Strain Distribution in GaN/AlGaN HEMT Structures. Microelectronics Reliability **2016**, 64, 541–546.
(23) Profijt, H. B.; van de Sanden, M. C. M.; Kessels, W. M. M. Substrate-Biasing during Plasma-Assisted Atomic Layer Deposition to Tailor Metal-Oxide Thin Film Growth. *J. Vac. Sci. Technol. A Vacuum, Surfaces, Film.* **2013**, *31* (1), 01A106.
(24) Puurunen, R. L. Surface Chemistry of Atomic Layer Deposition: A Case Study for the Trimethylaluminum/water Process. *J. Appl. Phys.* **2005**, *97* (12), 121301.
(25) Ritala, M. Atomic Layer Deposition - Basic Features, Advantages and Limitations, ESTC Short Course, 2014.
(26) Miikkulainen, V.; Leskelä, M.; Ritala, M.; Puurunen, R. L. Crystallinity of Inorganic Films Grown by Atomic Layer Deposition: Overview and General Trends. *J. Appl. Phys.* **2013**, *113* (2), 21301.
(27) Musschoot, J.; Deduytsche, D.; Poelman, H.; Haemers, J.; Van Meirhaeghe, R. L.; den Berghe, S.; Detavernier, C. Comparison of Thermal and Plasma-Enhanced ALD/CVD of Vanadium Pentoxide. *J. Electrochem. Soc.* **2009**, *156* (7), P122–P126.
(28) Van Bui, H.; Nguyen, M. D.; Wiggers, F. B.; Aarnink, A. A. I.; de Jong, M. P.; Kovalgin, A. Y. Self-Limiting Growth and Thickness-and Temperature-Dependence of Optical Constants of ALD AlN Thin Films. *ECS J. solid state Sci. Technol.* **2014**, *3* (4), P101–P106.
(29) Nepal, N.; Qadri, S. B.; Hite, J. K.; Mahadik, N. A.; Mastro, M. A.; Eddy, C. R. Epitaxial Growth of AlN Films via Plasma-Assisted Atomic Layer Epitaxy. *Appl. Phys. Lett.* **2013**, *103* (8), 082110.
(30) Bosund, M.; Sajavaara, T.; Laitinen, M.; Huhtio, T.; Putkonen, M.; Airaksinen, V. M.; Lipsanen, H. Properties of AlN Grown by Plasma Enhanced Atomic Layer Deposition. *Appl. Surf. Sci.* **2011**, *257* (17), 7827–7830.
(31) Perros, A. P.; Hakola, H.; Sajavaara, T.; Huhtio, T.; Lipsanen, H. Influence of Plasma Chemistry on Impurity Incorporation in AlN Prepared by Plasma Enhanced Atomic Layer Deposition. *J. Phys. D. Appl. Phys.* **2013**, *46* (50), 505502.
(32) Van Bui, H.; Wiggers, F. B.; Gupta, A.; Nguyen, M. D.; Aarnink, A. A. I.; de Jong, M. P.; Kovalgin, A. Y. Initial Growth, Refractive Index, and Crystallinity of Thermal and Plasma-Enhanced Atomic Layer Deposition AlN Films. *J. Vac. Sci. Technol. A Vacuum, Surfaces, Film.* **2015**, *33* (1), 01A111.
(33) Jokinen, J.; Haussalo, P.; Keinonen, J.; Ritala, M.; Riihelä, D.; Leskelä, M. Analysis of AlN Thin Films by Combining TOF-ERDA and NRB Techniques. *Thin Solid Films* **1996**, *289* (1–2), 159–165.

(34) Lee, Y. J.; Kang, S.-W. Growth of Aluminum Nitride Thin Films Prepared by Plasma-Enhanced Atomic Layer Deposition. *Thin Solid Films* **2004**, *446* (2), 227–231.
(35) Alevli, M.; Ozgit, C.; Donmez, I.; Biyikli, N. The Influence of N2/H2 and Ammonia N Source Materials on Optical and Structural Properties of AlN Films Grown by Plasma Enhanced Atomic Layer Deposition. *J. Cryst. Growth* **2011**, *335* (1), 51–57.
(36) Motamedi, P.; Cadien, K. Structural and Optical Characterization of Low-Temperature ALD Crystalline AlN. *J. Cryst. Growth* **2015**, *421*, 45–52.
(37) The Ioffe Physical-Technical Institute of the Russian Academy of Sciences, AlN, http://www.ioffe.ru/SVA/NSM/Semicond/AlN/index.html, (accessed Apr 5, 2018).
(38) Ozgit-Akgun, C.; Goldenberg, E.; Okyay, A. K.; Biyikli, N. Hollow Cathode Plasma-Assisted Atomic Layer Deposition of Crystalline AlN, GaN and AlxGa1-xN Thin Films at Low Temperatures. *J. Mater. Chem. C* **2014**, *2* (12), 2123.
(39) Newnham, R. E. *Properties of Materials: Anisotropy, Symmetry, Structure*; Oxford University Press on Demand, 2005.
(40) Aarik, J.; Kasikov, A.; Kirm, M.; Lange, S.; Uustare, T.; Mändar, H. Optical Properties of Crystalline Al2O3 Thin Films Grown by Atomic Layer Deposition. *Opt. Mater. Appl. Proc. SPIE Vol. 5946*, 2005; 594601.
(41) Matero, R.; Rahtu, A.; Ritala, M.; Leskelä, M.; Sajavaara, T. Effect of Water Dose on the Atomic Layer Deposition Rate of Oxide Thin Films. *Thin Solid Films* **2000**, *368* (1), 1–7.
(42) Groner, M. D.; Fabreguette, F. H.; Elam, J. W.; George, S. M. Low-Temperature Al2O3 Atomic Layer Deposition. *Chem. Mater.* **2004**, *16* (4), 639–645.
(43) Elliott, S. D.; Scarel, G.; Wiemer, C.; Fanciulli, M.; Pavia, G. Ozone-Based Atomic Layer Deposition of Alumina from TMA: Growth, Morphology, and Retention Mechanism. *Chem. Mater.* **2006**, *18* (8), 3764–3773.
(44) Van Bui, H.; Nguyen, M. D.; Wiggers, F. B.; Aarnink, a. a. I.; de Jong, M. P.; Kovalgin, a. Y. Self-Limiting Growth and Thickness- and Temperature- Dependence of Optical Constants of ALD AlN Thin Films. *ECS J. Solid State Sci. Technol.* **2014**, *3* (4), P101–P106.
(45) Mitchell, D. R. G.; Attard, D. J.; Triani, G. Transmission Electron Microscopy Studies of Atomic Layer Deposition TiO2 Films Grown on Silicon. *Thin Solid Films* **2003**, *441* (1), 85–95.
(46) Ho, M.-Y.; Gong, H.; Wilk, G. D.; Busch, B. W.; Green, M. L.; Voyles, P. M.; Muller, D. A.; Bude, M.; Lin, W. H.; See, A.; Loomans, M. E.; Lahiri, S. K.; Räisänen, P. I. Morphology and Crystallization Kinetics in HfO2 Thin Films Grown by Atomic Layer Deposition. *J. Appl. Phys.* **2003**, *93* (3), 1477–1481.
(47) Elers, K. E.; Saanila, V.; Li, W. M.; Soininen, P. J.; Kostamo, J. T.; Haukka, S.; Juhanoja, J.; Besling, W. F. A. Atomic Layer Deposition of WxN/TiN and WNxCy/TiN Nanolaminates. *Thin Solid Films* **2003**, *434* (1–2), 94–99.
(48) Jakschik, S.; Schroeder, U.; Hecht, T.; Gutsche, M.; Seidl, H.; Bartha, J. W. Crystallization Behavior of Thin ALD-Al2O3 Films. *Thin Solid Films* **2003**, *425* (1–2), 216–220.
(49) Gosset, L. G.; Damlencourt, J.; Renault, O.; Rouchon, D.; Holliger, P. Interface and Material Characterization of Thin Al2O3 Layers Deposited by ALD Using TMA/H2O. **2002**, *303*, 17–23.
(50) Klie, R. F.; Browning, N. D.; Chowdhuri, A. R.; Takoudis, C. G. Analysis of Ultrathin SiO2 Interface Layers in Chemical Vapor Deposition of Al2O3 on Si by in

Situ Scanning Transmission Electron Microscopy. *Appl. Phys. Lett.* **2003**, *83* (6), 1187–1189.
(51) Kim, S. K.; Hwang, C. S. Atomic-Layer-Deposited Al2O3 Thin Films with Thin SiO2 Layers Grown by in Situ O3 Oxidation. *J. Appl. Phys.* **2004**, *96* (4), 2323–2329.
(52) Zhang, L.; Jiang, H. C.; Liu, C.; Dong, J. W.; Chow, P. Annealing of Al2O3 Thin Films Prepared by Atomic Layer Deposition. *J. Phys. D. Appl. Phys.* **2007**, *40* (12), 3707–3713.
(53) Robertson, J.; Wallace, R. M. High-K Materials and Metal Gates for CMOS Applications. *Mater. Sci. Eng. R Reports* **2015**, *88*, 1–41.
(54) Broas, M.; Dong, H.; Graff, A.; Vuorinen, V.; Paul, A.; Laurila, T.; Paulasto-Kröckel, M. Thermodynamic and Composition-Structure Assessment of the Al-Au-Cu System at 150 C. *To be Publ.*
(55) Puurunen, R. L.; Sajavaara, T.; Santala, E.; Miikkulainen, V.; Saukkonen, T.; Laitinen, M.; Leskelä, M. Controlling the Crystallinity and Roughness of Atomic Layer Deposited Titanium Dioxide Films. *J. Nanosci. Nanotechnol.* **2011**, *11* (9), 8101–8107.
(56) Zeiss, SEM Column Schematic, https://www.zeiss.com/content/dam/Microscopy/Products/electron-microscopes/Gemini SEM/gemini_objective_lens.png, (accessed Apr 5, 2018).
(57) Waldrop, M. M. More than Moore. *Nature* **2016**, *530* (7589), 144–148.
(58) Williams, D. B.; Carter, C. B. Transmission Electron Microscopy: A Textbook for Materials Science. 2009. Springer.
(59) Inorganic Crystal Structure Database (ICSD), http://www2.fiz-karlsruhe.de/icsd_home.html, (accessed Apr 5, 2018).
(60) Elcombe, M. M.; Kealley, C. S.; Bhatia, V. K.; Thorogood, G. J.; Carter, D. J.; Avdeev, M.; Cortie, M. B. Determination of Martensite Structures of the Au7Cu 5Al4 and Au7Cu5.7Al3.3 Shape-Memory Alloys. *Acta Mater.* **2014**, *79*, 234–240.
(61) Cortie, M. B.; Kealley, C. S.; Bhatia, V.; Thorogood, G. J.; Elcombe, M. M.; Avdeev, M. High Temperature Transformations of the Au7Cu5Al 4 Shape-Memory Alloy. *J. Alloys Compd.* **2011**, *509* (8), 3502–3508.
(62) JEOL - Glossary of TEM Terms, Phase contrast, https://www.jeol.co.jp/en/words/emterms/search_result.html?keyword=phase%20contrast, (accessed Apr 5, 2018)
(63) Wang, Z. L. Transmission Electron Microscopy. Georgia Tech Course MSE6110 Lecture Slides. 2014.
(64) JEOL - Glossary of TEM Terms, k factor, https://www.jeol.co.jp/en/words/emterms/search_result.html?keyword=k factor (accessed Apr 4, 2018).
(65) Dong, H.; Vuorinen, V.; Broas, M.; Paulasto-Kröckel, M. Thermodynamic Reassessment of the Au-Pt-Sn System and Microstructural Evolution of the (AuSn)eut-Pt Interconnection. *J. Alloys Compd.* **2016**, *688*, 388–398.
(66) Poppitz, D.; Graff, A.; Simon-Najasek, M.; Broas, M.; Altmann, F. Strain Measurements at AlGaN/GaN HEMT Structures on Silicon Substrates. In *European Microscopy Congress Proceedings,* 2016; 678–679.
(67) Sintonen, S. Superhilarakenteiden Karakterisointi Röntgendiffraktio ja Röntgenheijastusmenetelmillä; Master's Thesis, Helsinki University of Technology, 2009.
(68) Husson, E.; Repelin, Y. Structural Studies of Transition Aluminas. Theta Alumina. *Eur. J. solid state Inorg. Chem.* **1996**, *33* (11), 1223–1231.

(69) Tiilikainen, J.; Tilli, J. M.; Bosund, V.; Mattila, M.; Hakkarainen, T.; Airaksinen, V.-M.; Lipsanen, H. Nonlinear Fitness-Space-Structure Adaptation and Principal Component Analysis in Genetic Algorithms: An Application to X-Ray Reflectivity Analysis. J. Phys. D. Appl. Phys. **2006**, 40 (1), 215.

(70) Laitinen, M.; Rossi, M.; Julin, J.; Sajavaara, T. Time-of-Flight – Energy Spectrometer for Elemental Depth Profiling – Jyväskylä Design. Nucl. Instruments Methods Phys. Res. Sect. B Beam Interact. with Mater. Atoms **2014**, 337, 55–61.

(71) Suni, T. Direct Wafer Bonding for MEMS and Microelectronics; Doctoral dissertation, VTT Publ. No. 609, 2006.

(72) Vermang, B.; Goverde, H.; Simons, V.; De Wolf, I.; Meersschaut, J.; Tanaka, S.; John, J.; Poortmans, J.; Mertens, R. A Study of Blister Formation in ALD Al2O3 Grown on Silicon. *38th IEEE Photovoltaic Specialists Conference (PVSC)*; IEEE, 2012; pp. 1135–1138.

(73) Mäntyoja, N. Evaluation of Characterization Methods for Cu-Sn Micro-Connects; Master's Thesis, Aalto University, 2016.

(74) Campbell, S. A. *Fabrication Engineering at the Micro-and Nanoscale*; The Oxford Series in Electrical and Computer Engineering, 2008.

(75) Lin, C.-Y.; Lu, F.-H. Oxidation Behavior of AlN Films at High Temperature under Controlled Atmosphere. *J. Eur. Ceram. Soc.* **2008**, *28* (3), 691–698.

(76) Perros, A.; Bosund, M.; Sajavaara, T.; Laitinen, M.; Sainiemi, L.; Huhtio, T.; Lipsanen, H. Plasma Etch Characteristics of Aluminum Nitride Mask Layers Grown by Low-Temperature Plasma Enhanced Atomic Layer Deposition in SF6 Based Plasmas. *J. Vac. Sci. Technol. A Vacuum, Surfaces, Film.* **2012**, *30* (1), 11504.

(77) Goerke, S.; Ziegler, M.; Ihring, A.; Dellith, J.; Undisz, A.; Diegel, M.; Anders, S.; Huebner, U.; Rettenmayr, M.; Meyer, H. G. Atomic Layer Deposition of AlN for Thin Membranes Using Trimethylaluminum and H2/N2 Plasma. *Appl. Surf. Sci.* **2015**, *338*, 35–41.

(78) Anderson, V. R.; Nepal, N.; Johnson, S. D.; Robinson, Z. R.; Nath, A.; Kozen, A. C.; Qadri, S. B.; DeMasi, A.; Hite, J. K.; Ludwig, K. F.; Eddy, C. R. Plasma-Assisted Atomic Layer Epitaxial Growth of Aluminum Nitride Studied with Real Time Grazing Angle Small Angle X-Ray Scattering. *J. Vac. Sci. Technol. A* **2017**, *35* (3), 31508.

(79) Beldarrain, O.; Duch, M.; Zabala, M.; Rafí, J. M.; González, M. B.; Campabadal, F. Blistering of Atomic Layer Deposition Al2O3 Layers Grown on Silicon and Its Effect on Metal–insulator–semiconductor Structures. *J. Vac. Sci. Technol. A Vacuum, Surfaces, Film.* **2013**, *31* (1), 01A128.

(80) Vermang, B.; Goverde, H.; Uruena, A.; Lorenz, A.; Cornagliotti, E.; Rothschild, A.; John, J.; Poortmans, J.; Mertens, R. Blistering in ALD Al2O3 Passivation Layers as Rear Contacting for Local Al BSF Si Solar Cells. *Sol. Energy Mater. Sol. Cells* **2012**, *101*, 204–209.

(81) Li, S.; Repo, P.; Von Gastrow, G.; Bao, Y.; Savin, H. Effect of ALD Reactants on Blistering of Aluminum Oxide Films on Crystalline Silicon. *Conf. Rec. IEEE Photovolt. Spec. Conf.,* 2013; 1265–1267.

(82) Hennen, L.; Granneman, E. H. a; Kessels, W. M. M. Analysis of Blister Formation in Spatial ALD Al2O3 for Silicon Surface Passivation. *38th IEEE Photovolt. Spec. Conf. (PVSC)*; IEEE, 2012; pp. 1049–1054.

(83) Xie, D.-G.; Wang, Z.-J.; Sun, J.; Li, J.; Ma, E.; Shan, Z.-W. In Situ Study of the Initiation of Hydrogen Bubbles at the Aluminium Metal/oxide Interface. *Nat. Mater.* **2015**, *14* (9), 1–6.

(84) Correa, G. C.; Bao, B.; Strandwitz, N. C. Chemical Stability of Titania and Alumina Thin Films Formed by Atomic Layer Deposition. *ACS Appl. Mater. Interfaces* **2015**, 14816–14820.
(85) Sadeghi-Tohidi, F.; Samet, D.; Graham, S.; Pierron, O. N. Comparison of the Cohesive and Delamination Fatigue Properties of Atomic-Layer-Deposited Alumina and Titania Ultrathin Protective Coatings Deposited at 200 °C. *Sci. Technol. Adv. Mater.* **2014**, *15* (1), 15003.
(86) Carcia, P. F.; McLean, R. S.; Li, Z. G.; Reilly, M. H.; Marshall, W. J. Permeability and Corrosion in ZrO2/Al2O3 Nanolaminate and Al2O3 Thin Films Grown by Atomic Layer Deposition on Polymers. *J. Vac. Sci. Technol. A Vacuum, Surfaces, Film.* **2012**, *30* (4), 041515.
(87) Abdulagatov, A. I.; Yan, Y.; Cooper, J. R.; Zhang, Y.; Gibbs, Z. M.; Cavanagh, A. S.; Yang, R. G.; Lee, Y. C.; George, S. M. Al_2O_3 and TiO_2 Atomic Layer Deposition on Copper for Water Corrosion Resistance. *ACS Appl. Mater. Interfaces* **2011**, *3* (12), 4593–4601.
(88) Kim, L. H.; Kim, K.; Park, S.; Jeong, Y. J.; Kim, H.; Chung, D. S.; Kim, S. H.; Park, C. E. Al2O3/TiO2 Nanolaminate Thin Film Encapsulation for Organic Thin Film Transistors via Plasma-Enhanced Atomic Layer Deposition. *ACS Appl. Mater. Interfaces* **2014**, *6* (9), 6731–6738.
(89) Puurunen, R. L.; Saarilahti, J.; Kattelus, H. Implementing ALD Layers in MEMS Processing. *ECS Trans.* **2007**, *11* (7), 3–14.
(90) Sammelselg, V.; Netšipailo, I.; Aidla, A.; Tarre, A.; Aarik, L.; Asari, J.; Ritslaid, P.; Aarik, J. Chemical Resistance of Thin Film Materials Based on Metal Oxides Grown by Atomic Layer Deposition. *Thin Solid Films* **2013**, *542*, 219–224.
(91) Kern, W.; Soc, J. E. The Evolution of Silicon Wafer Cleaning Technology. *J. Electrochem. Soc.* **1990**, *137* (6), 1887–1892.
(92) Kern, W. Cleaning Solutions Based on Hydrogen Peroxide for Use in Silicon Semiconductor Technology. *RCA Rev.* **1970**, *31*, 187–206.
(93) Paul, A.; Laurila, T.; Vuorinen, V.; Divinski, S. V. *Thermodynamics, Diffusion and the Kirkendall Effect in Solids*; Springer, 2014.
(94) De Yoreo, J. J.; Vekilov, P. G. Principles of Crystal Nucleation and Growth. *Rev. Mineral. geochemistry* **2003**, *54* (1), 57–93.
(95) Vekilov, P. G. Nucleation. *Cryst. Growth Des.* **2010**, *10* (12), 5007–5019.
(96) Wang, X.; Vlassak, J. J. Crystallization Kinetics of Amorphous NiTi Shape Memory Alloy Thin Films. *Scr. Mater.* **2006**, *54* (5), 925–930.
(97) Liu, K. T.; Duh, J. G. Kinetics of the Crystallization in Amorphous NiTi Thin Films. *J. Non. Cryst. Solids* **2007**, *353* (11–12), 1060–1064.
(98) Lee, H. J.; Ramirez, A. G. Crystallization and Phase Transformations in Amorphous NiTi Thin Films for Microelectromechanical Systems. *Appl. Phys. Lett.* **2004**, *85* (7), 1146–1148.
(99) Biswas, D.; Sinha, A. K.; Chakraborty, S. Optimization of Annealing Temperature for High-κ-Based Gate Oxides Using Differential Scanning Calorimetry. *J. Vac. Sci. Technol. B Nanotechnol. Microelectron.* **2015**, *33* (5), 052205.
(100) Levin, I.; Brandon, D. Metastable Alumina Polymorphs: Crystal Structures and Transition Sequences. *J. Am. Ceram. Soc.* **2005**, *81* (8), 1995–2012.
(101) Mousavi, S. J.; Hosseini, S. M.; Abolhassani, M. R.; Sebt, S. A. Calculation of the Structural, Electrical, and Optical Properties of κ-Al2O3 by Density Functional Theory. *Chinese J. Phys.* **2008**, *46* (2), 170–180.
(102) Cox, D. E.; Moodenbaugh, A. R.; Sleight, A. W.; Chen, H. Y. Structural Refinement of Neutron and X-Ray Data by the Rietveld Method: Application to Al2O3 and BiVO4. *Accuracy in Powder Diffraction: Proceedings of a Symposium on*

Accuracy in Powder Diffraction; US Department of Commerce, National Bureau of Standards, 1980, Vol. 567, p. 189.
(103) McHale, J. M.; Auroux, A.; Perrotta, A. J.; Navrotsky, A. Surface Energies and Thermodynamic Phase Stability in Nanocrystalline Aluminas. *Science* **1997**, *277* (5327), 788–789.
(104) Prokes, S. M.; Katz, M. B.; Twigg, M. E. Growth of Crystalline Al2O3 via Thermal Atomic Layer Deposition: Nanomaterial Phase Stabilization. *APL Mater.* **2014**, *2* (3), 1–6.
(105) Moriceau, H.; Rieutord, F.; Fournel, F.; Le Tiec, Y.; Di Cioccio, L.; Morales, C.; Charvet, A. M.; Deguet, C. Overview of Recent Direct Wafer Bonding Advances and Applications. *Adv. Nat. Sci. Nanosci. Nanotechnol.* **2010**, *1* (4).
(106) Leppäniemi, J.; Sippola, P.; Broas, M.; Aromaa, J.; Lipsanen, H.; Koskinen, J. Corrosion Protection of Steel with Multilayer Coatings: Improving the Sealing Properties of Physical Vapor Deposition CrN Coatings with Al2O3/TiO2 Atomic Layer Deposition Nanolaminates. *Thin Solid Films* **2017**, *627*, 59–68.

Aalto-DD 151/2018



ISBN 978-952-60-8129-8 (printed)
ISBN 978-952-60-8130-4 (pdf)
ISSN 1799-4934 (printed)
ISSN 1799-4942 (pdf)

Aalto University
School of Electrical Engineering
Department of Electrical Engineering and Automation
www.aalto.fi

BUSINESS +
ECONOMY

ART +
DESIGN +
ARCHITECTURE

SCIENCE +
TECHNOLOGY

CROSSOVER

DOCTORAL
DISSERTATIONS